J. Fluid Mech. (2021), *vol*. 915, A66, doi:10.1017/jfm.2021.90

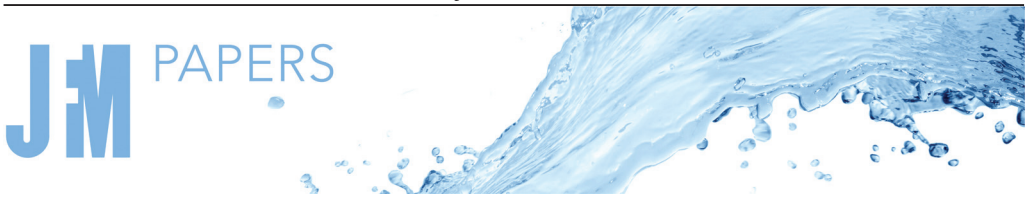

The engulfment of aqueous droplets on perfectly wetting oil layers

Callum Cuttle[1], Alice B. Thompson[2], Draga Pihler-Puzović[1] and Anne Juel[1],†

[1]MCND and Department of Physics and Astronomy, University of Manchester, Oxford Road, Manchester M13 9PL, UK

[2]MCND and Department of Mathematics, University of Manchester, Oxford Road, Manchester M13 9PL, UK

(Received 1 September 2020; revised 18 December 2020; accepted 22 January 2021)

Place a droplet of mineral oil on water and the oil will spread to cover the water surface in a thin film. In this paper we study the everted problem: an aqueous droplet deposited onto a deep layer of silicone oil. As it is energetically favourable for the oil phase to spread to cover the droplet surface completely, the droplet is ultimately engulfed in the oil layer. We present a detailed study of engulfment dynamics, from the instant the droplet impacts the oil surface until it finally sediments into the less dense oil. We study a broad range of droplet sizes (micrometric to millimetric) and oil kinematic viscosities (10^2–10^5 cSt), corresponding to a viscosity-dominated parameter regime. We find that droplet engulfment involves the rapid submersion of the droplet driven by capillary forces in the oil surface, followed by the much slower peeling of the droplet from the interface, to which it is adhered via a thin cloaking layer of oil formed during the earlier stage. The later peeling stage is driven by a combination of geometric constraints at the apparent contact line and gravity pulling on the droplet. Gravitational effects are therefore essential to complete engulfment, even for micrometric droplets. Furthermore, the opposing effects of geometry and gravity result in the longest engulfment times for droplets of intermediate size. Experiments at fixed droplet size reveal a power law dependence of engulfment time on oil kinematic viscosity, which we argue reflects the dynamical formation of the oil cloaking layer.

Key words: drops, capillary flows, multiphase flow

† Email address for correspondence: anne.juel@manchester.ac.uk

1. Introduction

The evolution of a droplet deposited on the surface of an immiscible liquid (sketched in figure 1*a*) is a conceptually simple problem with far-reaching societal impact, ranging from the everyday mixing of salad dressings to engineering applications, such as the cleaning of deep-sea oil spills (Fay 1969; Di Pietro, Huh & Cox 1978; Foda & Cox 1980; Kleidienst, Paul & Joye 2015) and pharmaceutical manufacture (Yeo, Basaran & Park 2003). The apparent simplicity of the problem is misleading, since the interfacial dynamics is governed by a complex interplay between viscous, gravitational and capillary forces acting at disparate length scales. For small (sub-millimetric) droplets, gravitational forces are generally neglected, with interfacial tensions γ between droplet, substrate and air phases playing the dominant role. The fate of the system then depends on how readily each liquid will wet and therefore spread upon the other; in particular, we may refer to the spreading coefficients $S_1 = \gamma_{da} - \gamma_{do} - \gamma_{oa}$ and $S_2 = \gamma_{oa} - \gamma_{do} - \gamma_{da}$, which respectively quantify how readily the substrate phase spreads on the droplet surface in the presence of air (subscripts o, d and a; later in the paper oil is used as the substrate) and *vice versa*. Broadly speaking, there are three possibilities at equilibrium (Berthier & Brakke 2012), as shown in figure 1(*b*). Perhaps the most commonly encountered situation is partial wetting between the droplet and the substrate (requiring both $S_1 < 0$ and $S_2 < 0$), as occurs for olive oil on water. In this case, the droplet will adopt a lens-shaped configuration at the surface of the substrate. The exact shape of the lens is determined by the balance of surface tensions at the contact line between the three phases, the Neumann construction (Buff & Saltsburg 1957), which is only possible if both spreading coefficients are negative. Alternatively, if $S_2 > 0$ the droplet will wet the substrate perfectly (e.g. mineral oil on water), in which case a Neumann construction is excluded and the droplet spreads to cover the substrate entirely since it is energetically favourable to do so (Langmuir 1933; Bergeron & Langevin 1996). The third possibility, which is the focus of this paper, is that the substrate wets the droplet perfectly ($S_1 > 0$; e.g. water on mineral oil). The substrate liquid then spreads to cover the droplet, engulfing it in the process (Berthier & Brakke 2012; Anand *et al.* 2015; Sanjay *et al.* 2019). Which of these three scenarios applies is not determined solely by the combination of liquids; the presence of surfactants, found ubiquitously in natural (and scientific) settings, is sufficient to alter the wetting properties of the phases, inhibiting spreading (Karapetsas, Craster & Matar 2011) or modifying the stability of liquid lenses (Phan *et al.* 2014). Hence, a thorough understanding of each scenario is required, and yet engulfment has been largely overlooked in previous research. In this paper, we therefore offer an in-depth study of the dynamics of droplet engulfment.

Gravitational effects are always present if there is any difference in density $\Delta\rho$ between the two liquid phases. Generally, gravitational effects are considered significant compared to capillarity for droplets larger than the capillary length $l_c = \sqrt{\gamma_{oa}/\Delta\rho g}$ (Vella 2015), typically a few mm, where g is the acceleration of gravity. For a partially wetting drop denser than the substrate phase, for example, the liquid lens configuration is only stable up to a critical droplet volume of order l_c^3 (with the exact value dependent on the Neumann construction) beyond which sinking is inevitable (Phan *et al.* 2012). By contrast, we find that for the engulfment of drops on perfectly wetting liquids, gravitational effects play a key role for even microscopic droplets.

Droplets or particles adhered or adsorbed to a liquid interface tend to deform the interface. This is generally due to a combination of gravitational effects – weight and buoyancy – as well as purely geometric constraints, as in the case of an interface meeting an adsorbed rigid particle at a fixed contact angle (Kralchevsky & Nagayama 2000; Vella & Mahadevan 2005; Galatola & Fournier 2014;

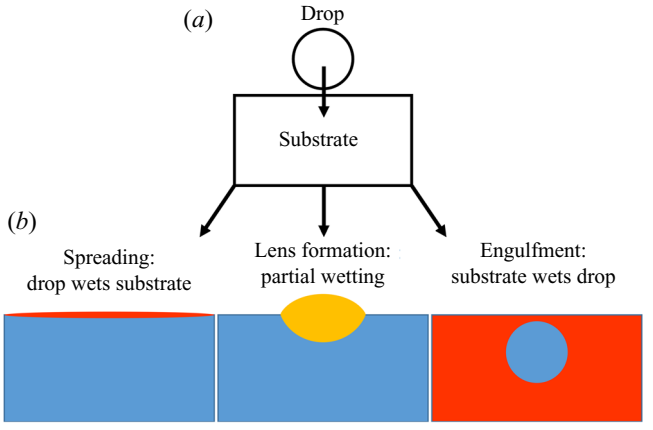

Figure 1. Schematic illustration of the possible equilibrium states of a droplet on an immiscible liquid substrate. (*a*) The droplet is deposited on the substrate. (*b*) Depending on wetting conditions, there are three general equilibrium states possible, neglecting gravity.

Carrasco-Fadanelli & Castillo 2019; Napoli & Goriely 2020). Away from equilibrium these deformations can drive capillary flows in the substrate phase as the interface evolves towards a minimal surface configuration, balancing hydrostatic pressures and curvature-induced capillary stresses. Such flows can generate interactions between droplets or particles at the interface, resulting in self-assembly and complex emergent behaviour (McGorty *et al.* 2010). For example, particle rafts of hydrophobic polymer beads on an air–water interface may collectively wrinkle like elastic solid sheets (Vella, Aussillous & Mahadevan 2004), while stainless steel beads aggregate to form structures too heavy to float at an air–oil interface, despite the individual beads being supported by capillarity (Protière *et al.* 2017). Similarly, interfacial colloidal suspensions may form 'soft crystals', organising themselves into a regular lattice structure (Park & Furst 2010).

The dynamics of liquid–liquid wetting, or spreading, has been studied in a number of geometries for perfectly wetting immiscible liquids. Oil reservoirs are brought into contact with air–water surfaces and allowed to spread within channels or circular baths (Camp & Berg 1987; Bergeron & Langevin 1996). More recently, droplet-on-droplet spreading has been studied due to applications in medicine and pharmaceuticals (Yeo *et al.* 2003). In all cases, the general features of spreading are similar, with the bulk of the spreading phase preceded by a molecularly thin precursor layer of the same fluid ((Bonn *et al.* 2009), see figure 2). Precursor layers spread rapidly over pristine surfaces, drawn out by a gradient in surface tension along the length of the film – a Marangoni flow (Fay 1969; Di Pietro *et al.* 1978; Foda & Cox 1980). Here, the disjoining pressure, arising from repulsive Van der Waals and other intermolecular interactions between the film surfaces, plays a role, modifying the free surface energy within the film (Harkins 1941; Brochard-Wyart *et al.* 1991; Bergeron & Langevin 1996). The advancing film is resisted by viscous dissipation.

The spreading of the bulk of the liquid once a precursor layer is established is a much slower process analogous to peeling dynamics, as illustrated in figure 2 (Lister, Peng & Neufeld 2013; Juel, Pihler-Puzović & Heil 2018). Just as a blister of fluid injected under a membrane grows by peeling the membrane away from the underlying substrate (figure 2*a*), a perfectly wetting droplet spreads by effectively peeling the two surfaces of the precursor film apart. Such peeling flows are dominated by stresses within a narrow peeling region which coincides with the apparent contact line at the rim of the spreading droplet (see figure 2*b*). Specifically, the dynamics of the flow is determined by a balance between

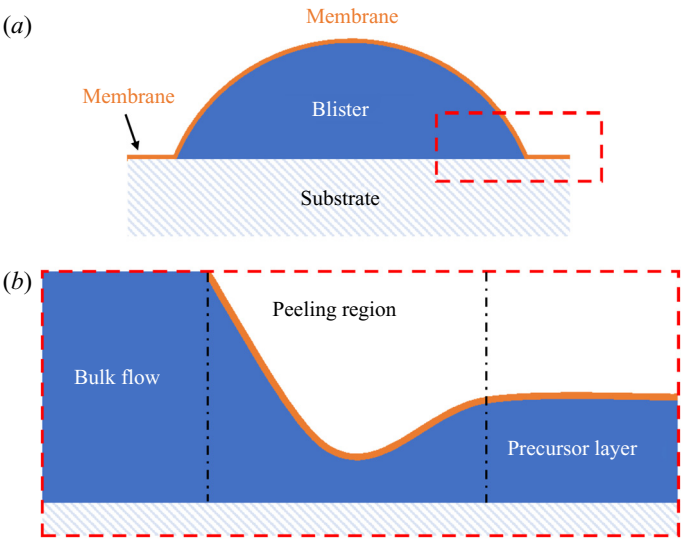

Figure 2. (*a*) Schematic diagram of a peeling flow for a blister of fluid under a membrane. (*b*) Close up of the boxed region in (*a*). The 'peeling region' around the edge of the blister separates the static precursor layer from the advancing bulk of the liquid phase.

capillary and viscous stresses which are focussed within the peeling region. In principle, the droplet should continue to spread into a 'pancake' shape of uniform thickness (i.e. a minimal surface), although in practice perfectly wetting droplets may exist as meta-stable lenses (pseudo-partial wetting) under the influence of the precursor layer (Kellay, Meunier & Binks 1992; Bergeron & Langevin 1996).

For a droplet of water, say, deposited on a layer of perfectly wetting oil, one may expect a comparable two-stage process by which the droplet is completely engulfed in oil (the equivalent of spreading). Indeed, analogous to the formation of precursor layers, a recent study (Sanjay *et al.* 2019) has shown that in this scenario the substrate phase will rapidly spread to cover the droplet surface entirely, establishing a thin 'cloaking' layer of oil. However, the majority of related studies have focussed on the deposition of aqueous droplets on liquid infused surfaces (LISs) – porous rigid substrates suffused with lubricant (generally oil), which demonstrate remarkably low friction and contact angle hysteresis (Sett *et al.* 2017; Solomon *et al.* 2017; McHale *et al.* 2019). Since the depth of lubricant is generally much less than the size of the droplet, total engulfment (that is, spreading) is not observed. Instead the droplet's weight is supported by the substrate, resting either on a stable film of lubricant or on the solid substrate itself, depending on the relative wetting properties of each phase (Smith *et al.* 2013), with the surrounding oil layer adopting a minimal surface configuration. At equilibrium, the surface of the cloaking layer must conform to the curvature of the droplet, subjecting the fluid within the cloak to a Laplace pressure. The equilibrium thickness of the cloak (typically tens of nm) is determined by balancing Laplace pressure in the fluid with disjoining pressure between the two surfaces, the latter being repulsive for perfectly wetting films (Anand *et al.* 2015; Schellenberger *et al.* 2015). Previous studies of cloaked droplets have therefore focussed predominantly on steady states of the system.

In this paper, we present an experimental study of an aqueous droplet engulfed by a deep layer of perfectly wetting, viscous oil on which the droplet is deposited. This scenario contrasts with droplets deposited on LISs; because the weight of the droplet cannot be

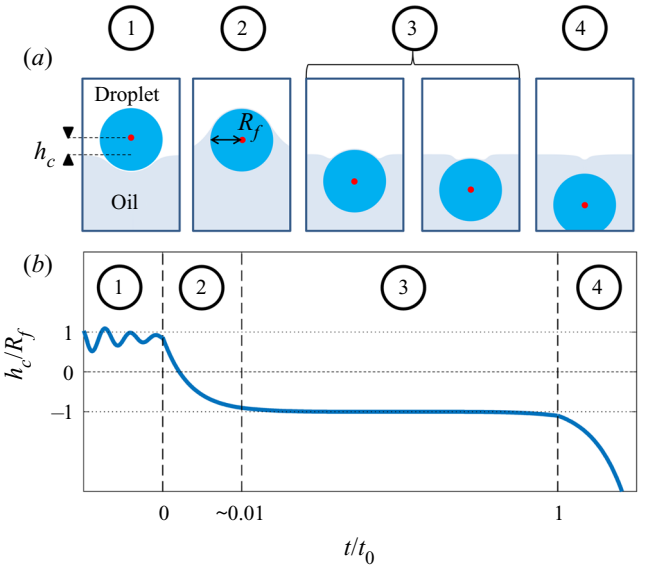

Figure 3. Overview of droplet engulfment. (*a*) Schematic diagram illustrating the four stages of engulfment. The red dot is the droplet's centroid. R_f is the droplet's in-flight radius. (*b*) Illustration of the dynamical process of engulfment, tracking the height h_c of the droplet centroid relative to the oil surface. Time is defined relative to the instant the air cushion ruptures ($t = 0$; start of stage 2) and $t = t_0$ is the instant when the droplet detaches from the oil surface (end of stage 3). The oscillations during stage 1 correspond to bouncing of the droplet after impact.

supported by a solid surface, total engulfment may take place – this type of unsteady dynamics has not been previously reported. We are primarily concerned with the spreading of the substrate phase (oil) over the droplet surface, and so will hereafter refer to a single spreading coefficient $S = \gamma_{da} - \gamma_{do} - \gamma_{oa}$, which was previously referred to as S_1.

The process by which the droplet is engulfed comprises four stages, as illustrated in figure 3. Stage 1 starts when the droplet impacts the oil layer, entraining a cushion of air upon which the droplet temporarily rests. The weight of the droplet (transferred via the air cushion) deforms the oil surface and drives air out of the cushion, bringing the oil and droplet surfaces closer together. As the separation between the two surfaces reaches a critical value of around ~100 nm, the attractive Van der Waals forces between the surfaces become dominant, rupturing the air cushion (Couder *et al.* 2005; Thoroddsen *et al.* 2012). We define the instant $t = 0$ at which oil first contacts the droplet as the start of stage 2 (figure 3*b*). Oil is then drawn upwards, spreading over the surface of the droplet (since $S > 0$); related studies suggest that the droplet is fully covered in a cloaking layer of oil early in stage 2 (Sanjay *et al.* 2019). As the droplet sinks, the local deformation of the oil layer around the droplet transitions from being deflected upwards (pulling the drop down) to being deflected downwards (resisting the downwards motion of the drop); the start of stage 3 is defined by the instant at which the oil surface around the droplet is undeflected. By contrast with droplets on LISs, during stage 3 the weight of the droplet acts to pull down on the oil surface, excluding a minimal surface configuration and driving continuous flows in the peeling region close to the apparent contact line. The cloaking layer of oil is thus gradually peeled away from the droplet surface, until the instant $t = t_0$ at which the droplet detaches from the oil surface. Detachment marks the start of stage 4, during which the droplet sinks into the slightly less dense oil. This final stage is sedimentation and is well

characterised: the droplet sinks under its own weight, resisted by buoyancy and viscous drag, predominantly within the oil phase (Hadamard 1911; Rybcznski 1911; Brenner 1962; Taylor & Acrivos 1964).

Since both impact (stage 1) and sedimentation (stage 4) are well understood (e.g. Brenner 1962; Thoroddsen *et al.* 2012), the focus of our study is the dynamics of engulfment during stages 2 and 3. Stage 3 is of particular interest as it dominates the dynamics, lasting for ∼99 % of the experimental duration t_0. In § 2 we describe our experimental methods. We present our results in § 3. By varying droplet size and substrate viscosity, we show in § 3.1 that the dynamics of early engulfment (stage 2) is determined by a competition between viscous and capillary effects. We also show evidence that a cloaking layer of oil covers the droplet early in stage 2. In § 3.2, we examine the evolution of gravitational and capillary forces acting on the droplet during late-time engulfment (stage 3). We find that viscous forces acting on the droplet are approximately equal to capillary forces exerted by the deformed oil surface throughout stage 3. Furthermore, we show that gravity plays a central role for even microscopic droplets. We discuss the slow spreading of oil over the droplet surface in terms of peeling dynamics, mediated by the oil cloak which acts as a precursor layer. The coupling between peeling dynamics and evolving gravitational and capillary forces yields the unexpected result that the time scale t_0 of engulfment varies non-monotonically with the size of the droplet, with droplets of intermediate size taking the longest time to detach from the oil surface. Experiments are also performed for droplets of fixed size on oils of different kinematic viscosity ν. We find that t_0 varies nonlinearly with ν, with a power law dependence which appears to be independent of droplet size. While the fate of our droplets is all but guaranteed (they must all sink eventually), our results reveal an unexpectedly rich dynamics leading to equilibrium.

2. Experimental methods

2.1. *Set-up and procedure*

The experimental set-up, shown schematically in figure 4(*a*), consists of an oil bath, onto which aqueous droplets were deposited. The oil phase was contained in bespoke open-topped cubic Perspex boxes of internal dimension $L = 40$ mm. Droplets of various sizes were used, quantified by their in-flight radius $R_f \approx \sqrt[3]{V/(4\pi/3)}$, where V is the droplet volume. The smallest droplets (microdroplets) had in-flight radii of tens of μm, while the radii of the larger macrodroplets were in the range $1 < R_f < 3$ mm. In all experiments, the droplet was deposited directly in the centre of the bath so as to maximise the distance between the droplet and the vessel walls. The size of the boxes was chosen to be much greater than that of the droplets ($L/R_f > 10$) in order to ensure that the vertical level of the oil surface was not increased significantly due to oil displaced by the droplet (the level rose by 2 % of R_f for the largest droplets studied). The reference level of the oil was measured after each experiment to account for any slight changes. In addition, since the droplets deformed a region of the oil surface of radius $\sim R_f$ around the droplet, the size of the box was sufficient to ensure that meniscus effects at the rigid walls were negligible. During stage 4 (sedimentation), we monitored the descent of the droplet away from the interface over a vertical distance of around one R_f. All droplets sedimented away from the oil surface without any clear evidence that a constant terminal velocity had been reached. The maximum measured Reynolds number during stage 4 was $Re = 1.2 \times 10^{-5}$, recorded for a drop with $R_f = 1.07$ mm deposited on oil with kinematic viscosity 100 cSt, and so we may assume Stokes' flow for all drops during stage 4. The drops sedimented

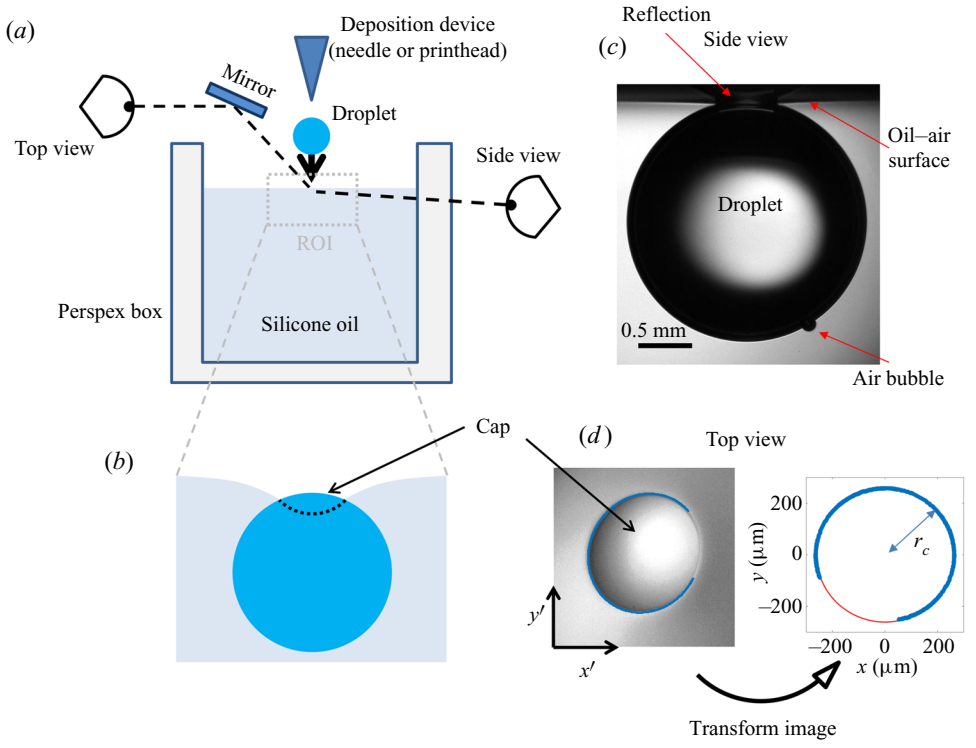

Figure 4. (*a*) Schematic diagram of the experimental set-up. The region of interest (ROI) is indicated. (*b*) Close-up schematic representation of the ROI during an experiment, showing the cap of the droplet visible above the oil bath surface. Panels (*c*) and (*d*) show typical experimental images in side and top views, respectively, during stage 3 of the experiment. Panel (*d*) shows the results of an image analysis routine which detects the edge of the droplet cap (left image; blue points): the image is distorted by the oblique viewing angle of the top view; a transformation procedure described in § 2.2 reconstructs the axisymmetric perimeter of the cap (right image; blue points), which is well approximated by a circle (red line), so that the radius r_c of the cap can be measured.

consistently more slowly than would be expected for a free droplet (Hadamard 1911; Rybcznski 1911) due to the increased drag resulting from long range interactions with the air–oil free surface as well as the vessel walls, with the magnitude of the additional drag force inversely proportional to the proximity of the boundary (Brenner 1962). While we can therefore not discount the drag due to vessel walls entirely, we expect the effect of the air–oil free surface to dominate due to the much greater proximity between the droplet and the surface.

Producing micro- and macrodroplets of reproducible sizes required two different deposition methods. Macrodroplets were deposited on the oil surface by dripping water from a deposition needle fed by a glass syringe acting as a reservoir, which was held above the oil bath. To generate a droplet, the plunger of the syringe was lightly tapped to initiate the formation of a pendant drop, which gradually grew due to a hydrostatic pressure-driven flow along the inclined needle. At a critical volume, the droplet detached from the needle, producing a droplet of reproducible volume. Capillary pressure at the outlet of the needle prevented any further drops from forming. We varied the in-flight radius of the macrodroplets by using deposition needles of different gauges. Droplets of size $R_f = 1.07 \pm 0.03$, 1.77 ± 0.02 and 2.17 ± 0.05 mm were produced using 30 gauge flat-tipped, and 21 and 17 gauge hypodermic needles, respectively. The largest drops used

ν (cSt)	Supplier	Composition	ρ_o (kg m^{-3})	γ_{oa} (mN m^{-1})
100	Silpak Inc.	PDMS	964	20.9
1000	Basildon Chemicals Ltd.	PDMS	970	20.3±0.7
30 000	Sigma-Aldrich	PDMS	976	21.3
100 000	Sigma-Aldrich	PDMS	976	21.3
1000	Sigma-Aldrich	PPMS	1090	21.1

Table 1. Physical properties of the silicone oils used in experiments. All quantities are quoted from suppliers, with the exception of the surface tension γ_{oa} of the 1000 cSt PDMS oil, which was measured using the pendant drop method. The value is in reasonable agreement with the supplier-quoted value of 21.1 mN m^{-1}. The density ρ_o and kinematic viscosity ν of each oil is also listed, along with the chemical composition. PDMS and PPMS refer to polydimethylsiloxane and polyphenylmethylsiloxane, respectively.

($R_f = 2.82 \pm 0.03$ mm) were produced by feeding water via a 30 gauge needle along the outer surface of a 17 mm diameter inclined cylindrical glass rod, allowing the water to drip from the lower edge of the rod. Microdroplets of $R_f = 38.6 \pm 0.4$ μm were produced using a piezoelectric drop-on-demand glass capillary printhead with a 120 μm diameter aperture (MJ-ABL-01-120-8MX; MicroFab Technologies Inc., USA). The printhead was powered with a waveform signal generated using a NI-DAQ (6251; National Instruments), amplified by a voltage amplifier (PZD 350A; Trek Inc., USA). The printhead could only produce water droplets of a particular volume, while the size of droplets which can be generated by dripping is limited by the capillary length (around 1 mm for water in air); hence, we were unable to investigate droplets with 39 μm $< R_f <$ 1 mm. For macrodroplets ($R_f >$ 1 mm), the needle (or rod) was positioned at a height $2R_f + 3$ mm above the oil surface such that the drops fell a distance 3 ± 1 mm before impact, resulting in an impact velocity of 24 ± 4 cm s^{-1}. The precise impact velocity did not affect the reproducibility of results (see Appendix A). For microdroplets, the printhead was positioned 11 ± 1 mm above the oil surface, impacting at 3 ± 0.4 m s^{-1}. Immediately after droplet deposition, the bath was covered with glass slides to protect the experiment from air currents and drifting dust particles within the laboratory.

We filled the bath with silicone oils of kinematic viscosity $10^2 \leq \nu \leq 10^5$ cSt. The decision to study this high-viscosity regime was based on preliminary results detailed in Appendix B. The physical properties of the oils are given in table 1. The majority of the oils used were polydimethylsiloxane (PDMS)-based fluids, all with densities ρ slightly lower than that of water. We also performed experiments with a 1000 cSt polyphenylmethylsiloxane (PPMS)-based oil with a density slightly greater than that of water. For oils of $\nu \leq 1000$ cSt, the baths were degassed under vacuum to remove any visible bubbles. For $\nu >$ 1000 cSt, meanwhile, the rupture of bubbles during degassing would leave films of oil which trapped more air as they settled, making degassing impractical. Instead, careful pouring was sufficient to ensure no air bubbles were trapped in such high-viscosity oils. The baths were covered and left to settle for 1 hour prior to experiments to ensure a level surface. Thorough cleaning of the Perspex boxes was required to ensure the oil surface was pristine. Prior to experiments, each box was cleaned with iso-propanol and then rinsed several times with deionised water before it was dried in a vacuum chamber. A similar cleaning procedure was followed for all components which came into direct contact with any liquid, e.g. syringes, printhead etc. Preliminary tests were performed with either water droplets doped with surfactant (washing-up liquid) beyond the critical micelle concentration, or Perspex boxes rubbed with paper towels to induce an electrostatic charge, both of which were sufficient to significantly alter

Liquid	ρ_d (kg m^{-3})	γ_{da} (mN m^{-1})	γ_{do} (mN m^{-1})	S (mN m^{-1})	ν (cSt)
Deionised water	1000	72.1 ± 0.9	39.5 ± 0.5	12.3 ± 1.2	1.00
PEDOT ink	1066	46.3 ± 0.9	19.7 ± 0.5	6.3 ± 1.2	5.86
Galden HT270	1850	20 ± 1	7 ± 1	-7 ± 2	11.7

Table 2. Physical properties of the liquids used to form the droplets in experiments. Densities ρ_d and kinematic viscosities ν are supplier-quoted or standard values. The droplet–air and droplet–oil surface tensions (γ_{do} and γ_{da}) were measured using pendant drop analysis. These values along with the oil–air surface tension γ_{oa} allow us to calculate the spreading coefficient $S = \gamma_{da} - \gamma_{do} - \gamma_{oa}$. Measurements of γ_{do} and γ_{oa} were taken using 1000 cSt PDMS oil.

experimental results. Both of these tests are too extreme to give any indication of the extent to which experiments were affected by surfactant or electrostatic effects. However, the reproducibility of our results (see § 3) suggests that our cleaning procedure at least resulted in consistent levels of any such perturbations.

We used three different fluids for the droplets: deionised water (Millipore 18.2 MΩ, Milli-Q), a proprietary PEDOT:PSS ink used in POLED printing (Cambridge Design Technology Ltd.) and a perfluorinated fluid (Galden HT270, Solvay), the physical properties of which are listed in table 2. Although PEDOT:PSS is a complex fluid, it is Newtonian at the low shear rates present in our experiments (Kant *et al.* 2017). The air–liquid and silicone oil–liquid interfacial tensions, γ_{da} and γ_{do}, were measured for each liquid in table 2 using the pendant drop method (Daerr & Mogne 2016). The 1000 cSt PDMS oil was used for measurements of γ_{do}. For practical reasons, measurements for viscosities $\nu > 1000$ cSt were not taken. However, the oils used are chemically similar, being PDMS or PPMS based, so that γ_{do} is approximately constant when varying ν, and values of γ and S measured using 1000 cSt PDMS oil are representative of all other oils used.

Table 2 also lists the substrate-on-droplet spreading coefficients S and densities ρ_d of the droplet liquids tested. Galden HT270 is the only one of the three liquids which is partially wetting on silicone oil, having $S < 0$. It is also considerably more dense than all of the oils used. Consistent with the discussion of § 1, we observed droplets of Galden HT270 deposited on 1000 cSt PDMS oil to form stable lenses up to $R_f \approx 1$ mm, around the capillary length $l_c = 1.6$ mm. Stable lenses were still present at the surface after >48 h. By contrast, for liquids with $S > 0$ (water; PEDOT ink) stable lens states were not observed, as oil naturally spread to cover the droplets completely (see § 3). Provided $\rho_o < \rho_d$, such a droplet should always eventually be engulfed and sink. This was the case for all our water droplets, including the microdroplets which all sank within a few minutes. See Appendix C for a discussion of the case when $\rho_o > \rho_d$.

2.2. *Visualisation*

Due to the disparate time scales involved, capturing the dynamics of each stage of engulfment (see figure 3) required a number of different imaging methods. During stage 2, around 90 % of the droplet's volume was submerged over ∼1 % of the total experiment duration t_0. The rapid vertical droplet motion was best imaged in side view (see figure 4*a*). Side view images were taken using a fast camera (Photron Fastcam Mini AX, 1024 × 1024 pixels, 1000–22 500 frames per second (f.p.s.) depending on oil viscosity) fitted with long-distance magnifying optics (Navitar) and a 50 mm f/1.4 lens for macrodroplets, or a 10× microscope objective (Mitutoyo) for microdroplets. To avoid imaging through the oil

meniscus, the side view camera was inclined upwards relative to the horizontal at an angle of 2°, which is small enough to not distort the image significantly. To capture the droplet impact dynamics in stage 1, a similar method was employed with the camera inclined downwards to image above the oil surface.

During stage 3, the droplet remained suspended beneath the oil surface, as shown schematically in figure 4(*b*), sinking slowly whilst oil spread to cover the droplet over ∼99 % of t_0. Stage 3 was imaged simultaneously in side view (fast camera set-up described for stage 2, recording at 50 f.p.s.), as well as in top view, looking down onto the upper surfaces of the droplet and surrounding oil. Figure 4(*c*) shows a typical experimental side view image for a macrodroplet ($R_f = 1.07$ mm); the small air bubble visible on the underside of the droplet is a remnant of the air entrained by the drop upon impact (Thoroddsen *et al.* 2012; Tran *et al.* 2013). The oil surface curves down towards the droplet, appearing to meet the droplet at a sharp angle. When viewed from above, this gave the impression of a 'cap'-like region of the droplet protruding above the oil surface with a well-defined perimeter. Figure 4(*d*) shows a typical image of this cap, recorded by the top view camera. Top view images were taken via a charge-coupled device camera (Pixelink, 1280 × 1024 pixels, 5–50 f.p.s.), fitted with a long-distance assembly along with either a 5× or 10× microscope objective (Mitutoyo) for macro- and microdroplets, respectively. The droplet was back lit in both directions using LED lamps diffused through opalescent acrylic. Side view recordings for stage 3 also captured part of stage 4 (sedimentation).

In all experiments, the deposition device used (needle, glass rod or printhead) obscured the view directly above the droplet. Imaging from below, through the Perspex box, oil and droplet, produced refractive distortions of the image, hindering quantitative image analysis. We therefore imaged from above at an oblique angle, via an inclined mirror (figure 4*a*). This produced significantly distorted images, as shown in figure 4(*d*), where the circular cap of the drop protruding from the oil bath appears 'egg shaped'. To correct for this distortion, we imaged a precision linear micro-scale (1 mm; 200 µm bars at 100 µm intervals) in top view prior to each experiment. We then took a set of points (x', y') from the distorted image of the micro-scale, corresponding to a set of points (x, y) of known relative dimensions in the physical plane. The points (x', y') could then be transformed into (x, y) via rotation, shear and rescaling transformations. The same set of transformations could then be applied to reconstruct any top view image in the physical plane. The right image of figure 4(*d*) shows the result of this procedure applied to an experimental image; a circular cap perimeter has been recovered, with accurate dimensional units allowing us to measure the radius r_c of the cap in each frame. To validate the procedure, we applied the method to top view images of printed text or specks of dust on microscope slides. We compared the reconstructed images to undistorted images of the same object recorded directly from below. Angles and lengths were recovered to within 1 ° and 1 % of the true values, respectively. This imaging procedure was only used during the later stage 3 of engulfment, over which the droplet descends by around $0.1R_f$; hence, the contact line only moves very slightly relative to the imaging plane of reference and the quality of reconstruction is not significantly affected.

2.3. *Evaporation*

The evaporation of water droplets was monitored throughout experiments by estimating the droplets' instantaneous volume from side view (macrodroplets) or top view (microdroplets) images. This was done by fitting a circular profile to a droplet's perimeter and comparing the instantaneous radius $R(t)$ to the in-flight radius R_f. For macrodroplets, the maximum recorded evaporative volume loss (defined as $1 - (R(t_0)/R_f)^3$) was 3 %,

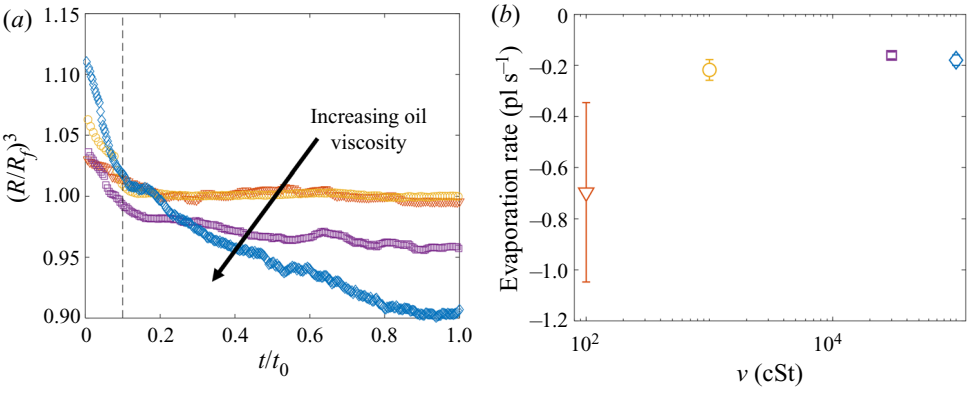

Figure 5. Evaporation of microdroplets. (*a*) Volume loss quantified by the measured radius $(R/R_f)^3$, where R is the measured radius at time t and $R_f = 38.6 \pm 0.4$ μm is the in-flight radius. Engulfment occurred over times t_0 ranging from 0.7 s for drops on 100 cSt oil to 160 s on 10^5 cSt oil. (*b*) The evaporation rate is calculated by taking a linear fit to the data in (*a*) for times $t/t_0 > 0.1$ (dashed line in (*a*)).

in the case of a 1.07 mm drop deposited on 10^5 cSt oil ($t_0 \approx 1$ h). All macrodroplet experiments were conducted in ambient laboratory conditions of $21 \pm 1\,^{\circ}$C at a relative humidity of $30\,\% < \phi < 50\,\%$, as read from a digital thermo-hygrometer beside the apparatus. Repeat trials on different days suggested variations in humidity over this range did not significantly affect the results. For microdroplets, however, significant (or complete) evaporation was observed over experimental times in ambient conditions, and so experiments were instead performed in a sealed humidity chamber: a modified fume hood housing the experimental apparatus, in which the relative humidity was maintained in the range $80\,\% < \phi < 90\,\%$. Figure 5(*a*) shows the time evolution of normalised droplet volume $(R(t)/R_f)^3$ for droplets with $R_f = 38.6$ μm over the full range of ν tested. Times have been normalised by the total experimental duration t_0 (see § 2.2). At early times ($t < 0.1t_0$) the shape of the droplet is distorted both physically and optically due to being compressed vertically by capillary stresses, as well as the deformed oil surface acting as a concave lens. Consequently, the measured radius $R(t)$ is initially $> R_f$. This effect subsides, and at later times the droplet volume can be seen to decrease approximately linearly with time in all cases. A linear fit to these data indicates that the evaporation rate is approximately constant at around -0.2×10^{-12} l s^{-1} for all ν (figure 5*b*). (We note that the point at 100 cSt is unreliable due to the relatively short experimental time $t_0 < 1$ s.) The 10^5 cSt case had by far the longest experimental duration of $t_0 \approx 160$ s, and therefore the greatest absolute evaporation ($\sim$10 % of the initial volume). In § 3 the majority of the discussion focusses on droplets deposited on 1000 cSt oil, for which evaporative losses were around 0.3 % and 1 % for macro- and microdrops, respectively.

We note that in ambient conditions, one would expect the rate of evaporation to be proportional to the surface area of the droplet, and therefore to vary in time. The fact that we observe a roughly constant rate of evaporation throughout our experiments may reflect the fact that the decrease in droplet volume over any experiment is small ($<$10 %); the surface area of each droplet is therefore roughly constant, yielding a fixed rate of evaporation. In addition, as droplets are engulfed and submerged, their 'ambient surroundings' (i.e. the oil and air phases) are continuously evolving, which may also affect the rate of evaporation.

3. Results

3.1. *Early-time engulfment*

During early-time engulfment, or stage 2, the droplet is rapidly submerged beneath the oil layer. We begin in § 3.1.1 by identifying the onset of engulfment (the start of stage 2) by studying impact. We also identify the transition from stage 2 to stage 3 in terms of the evolving oil surface configuration around the droplet. In § 3.1.2 we then investigate the effect of varying droplet size and substrate viscosity on the dynamics of early-time engulfment. Our results suggest the droplet is cloaked in a thin layer of oil early in stage 2, which we discuss further in § 3.1.3.

3.1.1. *Start and end of early-time engulfment*

Figure 6(*a*) shows a sequence of side view images of a droplet with $R_f = 1.07$ mm during stages 1 ($t < 0$) and 2 ($0 < t \lesssim 1$ s) of an experiment on oil of viscosity $\nu = 1000$ cSt. This droplet impacted at a speed $U_f = 50$ cm s^{-1} (although we note that the dynamics of stages 2 and 3 was independent of U_f over the range studied; see Appendix A). The dynamics is shown in figure 6(*b*) in terms of the maximum height H_a of the droplet relative to the far-field oil surface (labelled in figure 6*a*). Stage 1 begins with the impact of the droplet at $t = -1.63$ s. Immediately after ($t = -1.62$ s), the droplet bounces and is compressed as it again impacts the oil ($t = -1.58$ s). These bounces are visible as a scatter of data points at $t < -1.5$ s in figure 6(*b*), which are plotted at timesteps similar to the duration of individual bounces. The basic mechanism for droplet bouncing is similar to that identified for droplets impacting superhydrophobic micro-column surfaces (Richard & Quéré 2000); an air film trapped beneath the droplet prevents wetting, and hence the kinetic energy of impact is transferred predominantly into droplet surface energy, allowing the droplet to spring back into shape and bounce. In our experiments, the substrate may also deform, resulting in a recoil in the oil surface which likely modifies bouncing. During this early stage, surface capillary waves generated upon each impact deform the droplet, producing the light-bulb shapes visible at $t \leq -1.58$ s in figure 6(*a*). The kinetic energy of the droplet is dissipated by bulk viscous stresses within the droplet and oil phases, which oppose the displacement flows driven by the deformations of each surface. After a few (<3) bounces, the droplet comes to rest on a cushion of air entrained beneath the droplet during the final impact. Small oscillations persist on the droplet's surface, visible for around 0.1 s, after which the droplet appears static while the air cushion drains. The dark band visible at the base of the droplet ($t < 0$ in figure 6*a*) is the shadow cast within a crater in the oil surface in which the droplet sits (hence, $H_a/2R_f < 1$).

Stage 2 begins at the instant $t = 0$, which we identify by the sudden onset of surface capillary waves (distinct from those observed immediately after impact), driven by the spreading of oil films over the droplet after the air cushion ruptures. The effect of these waves on the height H_a of the droplet cap is visible as a series of peaks in the inset of figure 6(*b*), which shows the data at reduced timesteps close to $t = 0$. Converging capillary waves meeting at the apex of the droplet produce the unusual peaked shape visible in figure 6(*a*) at $t = 6$ ms. Similar deformations are observed for water droplets gently brought into contact with thin films of PDMS oil (Carlson *et al.* 2013). By $t = 31$ ms, the oil surface local to the droplet has inverted: the crater (dark band) has evolved to an upward-inflected skirt of oil. This inversion signals a reversal in the direction of the capillary forces acting on the droplet due to the deformed oil surface: in stage 1, the droplet's weight is supported, while in stage 2 the droplet is pulled down. As the droplet sinks, the oil surface flattens around the droplet (e.g. figure 6*a*, $t = 0.18$ s). The vertical

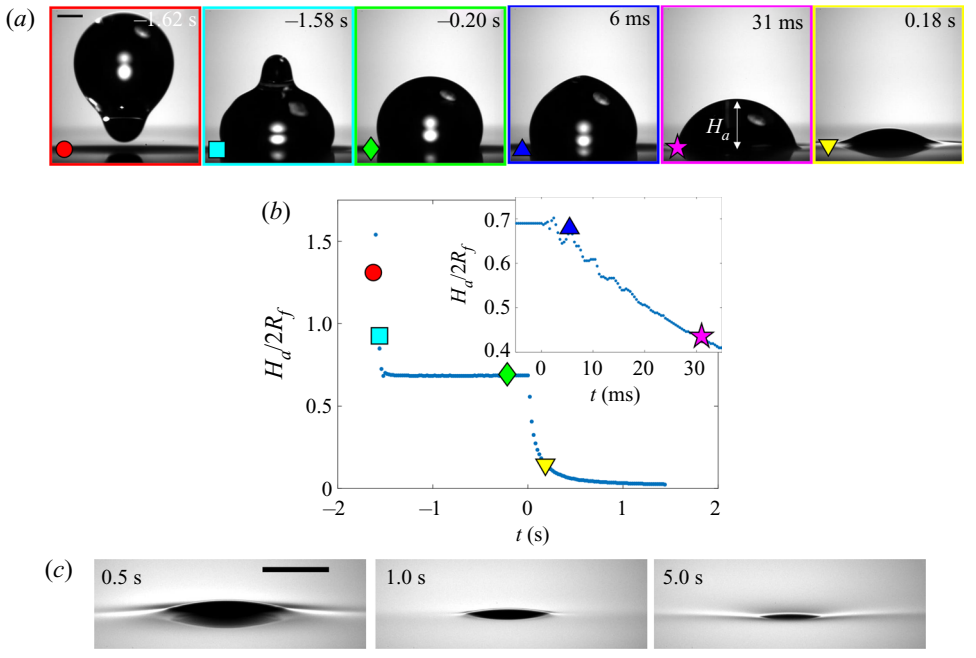

Figure 6. Early-time engulfment dynamics. (*a*) Time sequence of experimental images depicting stages 1 and 2 of engulfment for a droplet with $R_f = 1.07$ mm deposited onto 1000 cSt PDMS oil. Immediately before impact, the droplet was travelling at speed $U_f = 50$ cm s^{-1}. Times are measured relative to the instant at which the air cushion beneath the drop ruptures. The scale bar is 0.5 mm. The maximum height H_a of the droplet above the far-field oil level is labelled. The first image ($t = -1.62$ s) was taken as the droplet bounced immediately after impact. (*b*) Time evolution of the normalised height $H_a/2R_f$ of the droplet cap above the oil surface (defined in (*a*)). Inset: close-up of the data, showing the onset of capillary waves at $t = 0$; the precision of the measurement of $t = 0$ is limited by the frame rate, in this case 2400 f.p.s. Large markers correspond to the images shown in (*a*), with consistent colours used for markers and image borders. (*c*) Images of a droplet from late in stage 2 ($t = 0.5$ s) until early in stage 3 ($t = 5.0$ s). These images were taken during a repeat of the experiment shown in (*a*), imaged at greater magnification to enhance spatial resolution. Deformation to the oil surface is visible as grey streaks either side of the dark droplet cap. The scale bar is 0.5 mm.

component of the capillary forces acting on the droplet therefore reduces and the droplet's descent continually slows. At around $t = 1.0$ s, the oil surface is almost level around the droplet, as shown in the magnified images of figure 6(*c*). By $t = 5.0$ s, however, the oil layer is again deformed, although the surface now curves downwards towards the drop, rather than inflecting upwards. Once again, this inversion of the oil surface corresponds to a reversal in the direction of capillary forces, with the oil surface tension now acting to resist the downwards motion of the droplet. We define this transition, occurring around $t = 1.0$ s for the drops in figure 6, as the start of stage 3 (see § 3.2).

3.1.2. *Effect of droplet size and oil viscosity on early-time engulfment*

Figures 7(*a*) and 7(*b*) show stage 2 for macro- and microdroplets, respectively, imaged from just below the oil surface. Stage 1 ($t < 0$) was studied for macrodroplets only, because for microdroplets stage 2 initiated immediately upon impact, to within our experimental time resolution of 5×10^{-5} s. We attribute this to rapid drainage of the air cushion, which occurs over shorter time scales for smaller droplets (Couder *et al.* 2005). Hence, no image is shown in figure 7(*b*) at $t < 0$ for microdroplets. In stage 2, a qualitatively similar

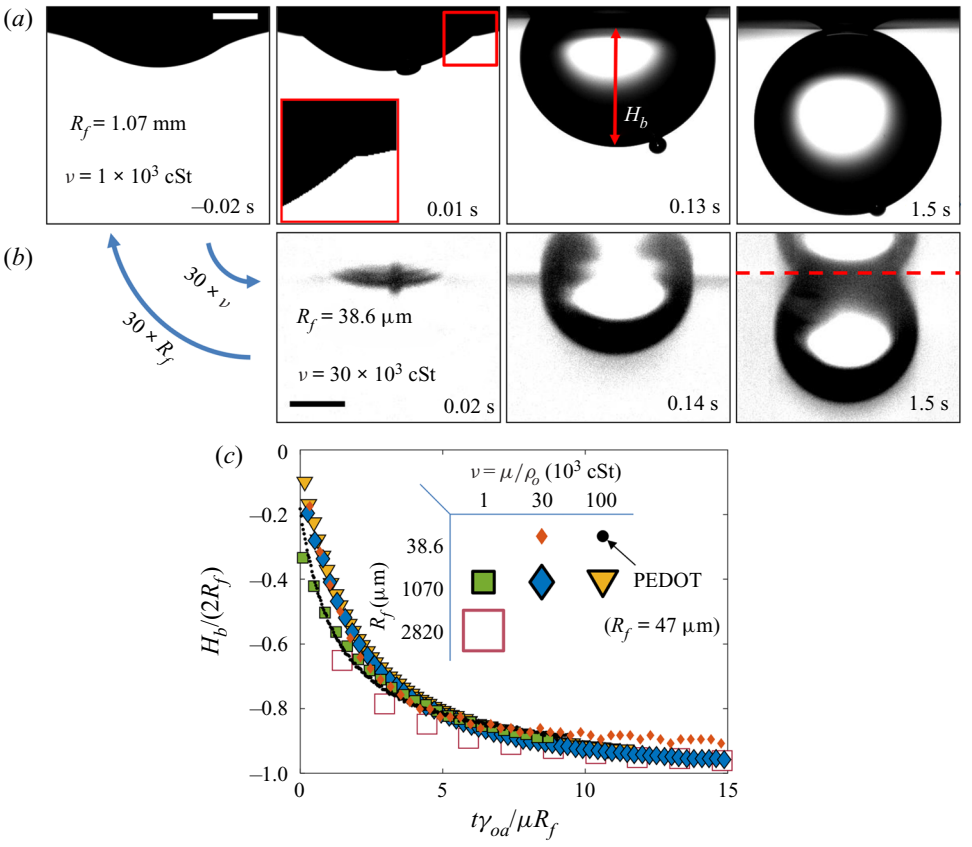

Figure 7. Effect of oil viscosity and drop size on early-time engulfment. (*a*,*b*) Experimental images for (*a*) a macrodroplet with $R_f = 1.07$ mm sinking into 1000 cSt oil and (*b*) a microdroplet with $R_f = 38.6$ μm sinking into 30 000 cSt oil. The depth H_b of the drop below the initial oil–air surface is labelled. The far-field oil level is indicated by dashed lines in images at $t = 0.13$–0.14 s; in (*b*) the droplet's reflection is visible in the oil surface. The small air bubbles visible are left by the rupture of the air cushion at $t = 0$. The minimum height H_b of the droplet relative to the far-field oil level is labelled in (*a*). Times are measured relative to the rupture of the air cushion. Inset: a binarised enlarged image of the region indicated by the red box in (*a*). (*c*) The rescaled depth $H_b/2R_f$ during early engulfment, as a function of rescaled time t/τ_γ for drops of various sizes over a range of oil viscosities. The visco-capillary time scale is $\tau_\gamma = \mu R_f/\gamma_{oa}$; $\mu = \nu\rho_o$ and γ_{oa} are, respectively, the dynamic viscosity and liquid-vapour surface tension of the oil phase. The legend indicates the droplet in-flight radius and oil viscosity for each data set. The black dots are data for a PEDOT ink microdroplet ($R_f = 47$ μm).

dynamics is observed for both droplets. They each entrain a (relatively) small air bubble (a remnant of the air cushion), and both are squeezed vertically by viscous resistance in the displaced oil phase. Note that for the macrodroplet at $t = 0.01$ s, the oil surface curves in towards the droplet (see inset of figure 7*a*), consistent with oil spreading upwards over the droplet early in stage 2.

Both droplets in figure 7(*a*,*b*) sink over similar time scales, as can be seen from the timestamps on each image. We note also that the macrodroplet has an in-flight radius, R_f, 30 times larger than that of the microdroplet, while the microdroplet sinks into oil which is 30 times more viscous. This evidence suggests a visco-capillary time scale for stage 2, $\tau_\gamma = \mu R_f/\gamma_{oa}$, where $\mu = \rho_o\nu$ is the dynamic viscosity of the oil. (Note that γ_{oa} and ρ_o are approximately constant for all PDMS oils; see table 1.) Figure 7(*c*) shows the dynamics of stage 2, in terms of the minimum height H_b of the droplet relative

to the oil far-field level (see figure 7*a*), for viscosities and droplet radii in the ranges 1000 cSt $\leq \nu \leq 10^5$ cSt, and 38.6 μm $\leq R_f \leq$ 2.82 mm. By rescaling t by τ_γ and H_b by $2R_f$, we are able to achieve a good collapse of these data. Physically, this suggests that sinking in stage 2 is driven by capillary stresses $\sim\gamma_{oa}/R_f$ and opposed by bulk viscous stresses resisting the displacement of oil. Moreover, the data for a microdroplet ($R_f = 47$ μm) of PEDOT on 10^5 cSt oil (black dots) also collapse reasonably well onto the same curve. This suggests early-time engulfment is largely independent of the oil-droplet spreading coefficient S, which is roughly twice as large for water compared with PEDOT (table 2), being governed instead by the oil properties and droplet size.

3.1.3. *Cloaking of the aqueous droplet on oil*

In a related study of water droplets brought into contact with thin layers of silicone oil, Carlson *et al.* (2013) note that the droplets should be entirely covered in a thin cloaking layer of oil (since $S > 0$). Furthermore, Carlson *et al.* (2013) suggest that the cloak should form over a time scale τ_γ, the same time scale observed for stage 2 in our experiments ($\sim 20\tau_\gamma$). Indeed, Sanjay *et al.* (2019) recently found, in experiments similar to our own, that water macrodroplets on 20 and 200 cSt PDMS oils are completely cloaked within the first 10 ms of stage 2. Given these results, it is reasonable to conclude that our droplets are likely cloaked early in stage 2. This is consistent with the observation that the early-time dynamic scaling in § 3.1.2 is independent of S; once the cloaking layer has covered the entire droplet surface, the exact differences in surface tension components (i.e. the value of S) become inconsequential. In the following sections, we extend the discussion of cloaking layers, examining their influence on the dynamics of late-time engulfment.

3.2. *Late-time engulfment*

3.2.1. *Physical description*

At the start of stage 3, the droplet hangs beneath the oil surface, as sketched in figure 8(*a*). The weight of the droplet pulls down on the oil surface, which is adhered to the droplet surface via the thin cloaking layer of oil (see Appendix D for further experimental evidence of adhesive stresses in cloaking layers). Because the droplet is only slightly more dense than the oil, the majority of the droplet's weight is matched by the opposing buoyant force, equal to the weight of the displaced oil. Deformations in the oil surface generate capillary stresses, which pull upwards on the drop; in addition, gradients in curvature along the deformed surface drive a flow which peels the cloak from the droplet surface. Significant viscous stresses are then present within the peeling region coinciding with the apparent contact line (see inset of figure 8*a*), as with related peeling flows.

Since the droplets descend a distance $\sim 0.1R_f$ over roughly t_0 during stage 3, we estimate the characteristic Reynolds number as $Re = 0.2R_f^2/t_0\nu$ (again taking the in-flight droplet diameter $2R_f$ as the length scale). For all experiments $10^{-14} \lesssim Re \lesssim 10^{-7}$ during stage 3, and we are therefore in the Stokes flow regime. As such, the flows associated with engulfment – that is, the peeling of the cloak and the sinking of the droplet – are driven by the net effect of non-viscous stresses (gravity and capillarity). Viscous stresses then act to oppose any resultant flows and ensure a net force balance at all points.

In the rest of § 3, we examine the effects of gravity, capillarity, and viscosity on the slow engulfment dynamics of stage 3. Our results point to two distinct features which complicate the dynamics of engulfment. First, we find that both gravitational and capillary forces, which drive engulfment in stage 3, evolve continuously over time. Therefore, their

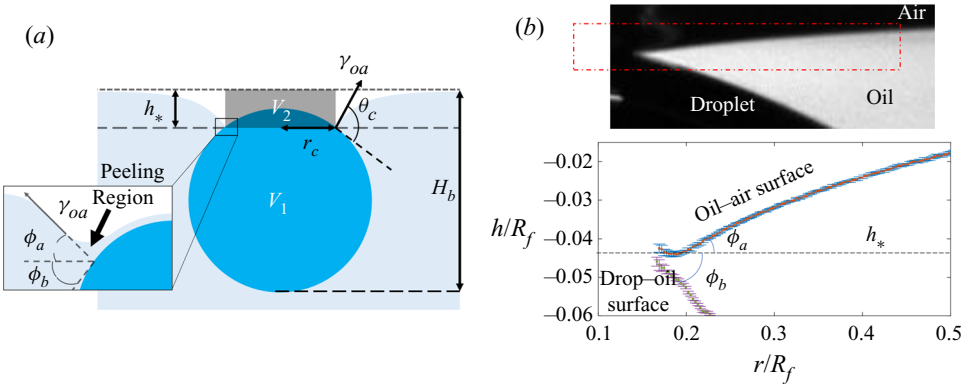

Figure 8. (*a*) Schematic illustration of the system during stage 3. The oil and droplet surfaces meet at an apparent contact line, a height h_* below the far-field oil level, which encircles a cap-like region of radius r_c. Inset: viscous resistance is concentrated in a small peeling region close to the apparent contact line. (*b*) Top: close-up side view image in the region close to the apparent contact line for a droplet with $R_f = 2.17$ mm on 1000 cSt PDMS oil, taken at $t = 0.78t_0 = 54.5$ s. Bottom: profiles of each surface extracted from the boxed region of the image. The apparent inclinations ϕ_a and ϕ_b of each surface relative to the horizontal are labelled; respectively, ϕ_a and ϕ_b are measured at the points of maximum and minimum gradient along fifth-order polynomials fitted to data points from each surface. Sub-pixel precision was achieved by fitting hyperbolic tangent intensity profiles along each column of pixels; error bars are the corresponding parameter uncertainties from the nonlinear fitting routine.

relative importance cannot be described by experimental parameters alone, for instance by referring to the Bond number $Bo = (\rho_d - \rho_o)gR_f^2/\gamma_{oa}$; we must also consider the evolving geometry. Secondly, viscous stresses act not only to oppose the sinking of the droplet, but also determine the peeling dynamics at the apparent contact line, and their effect on the engulfment dynamics is therefore non-trivial. As such, no obvious rescaling of the kind applied to the dynamics of stage 2 (see figure 7) emerges for stage 3. We therefore present and interpret the following results without reference to simplified models which we believe are inappropriate for a system of such complexity.

3.2.2. *Effect of droplet size*

The time evolution of stage 3 of engulfment is shown in figures 9(*a*) and 9(*b*), for drops of all in-flight radii R_f studied, in terms of the depth H_b of the droplet relative to the far-field oil level and the radius r_c of the cloaked droplet cap (see figure 8*a*). These experiments were conducted using 1000 cSt PDMS oil. During stage 3, the rate at which a droplet is engulfed varies continuously, both in terms of $H_b(t)$ and $r_c(t)$. For all droplets, we observe an initial decrease in the rate of engulfment. For macrodrops, this slowing persists for around half of the experimental duration t_0, reaching an inflection where the gradients of $r_c(t)$ and $H_b(t)$ take minimum values, before the rate of engulfment begins to increase up to the instant of detachment from the oil surface, t_0. For the microdroplet, however, there is no clear evidence of a final increase in the rate of engulfment, with engulfment appearing to slow continually throughout stage 3. We note, however, that for microdroplets ($R_f = 38.6$ μm), measurements of the cap radius r_c could only be taken before it reduced to around 1 μm. Beyond this point, the perimeter of the cap became too faint to distinguish visually, disappearing entirely at around $t \approx t_0/2$, and becoming once again visible as a small bright spot from $t \approx 3t_0/4$. The instant of detachment t_0 (large symbol in inset of

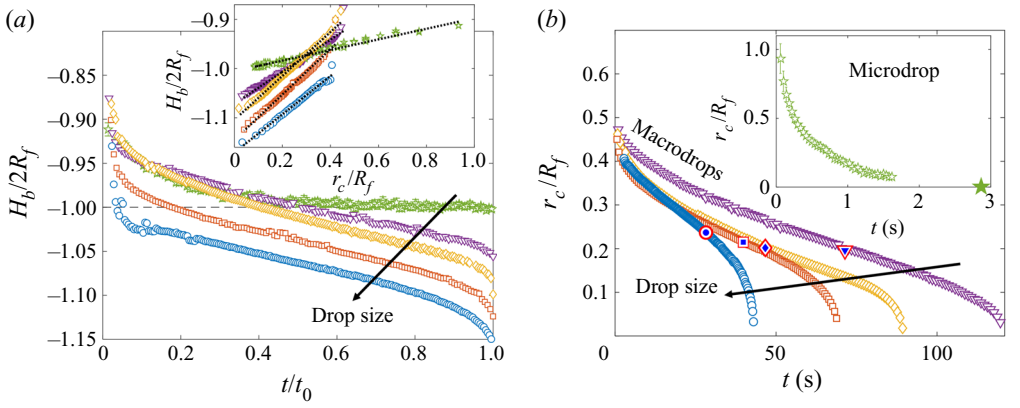

Figure 9. (*a*,*b*) Sinking and spreading dynamics for drops of various in-flight radii R_f, on 1000 cSt PDMS oil. Each experiment was repeated at least three times, with the total engulfment time t_0 reproducible to within ±6 %. Due to the increasing spread of data late in stage 3 ($t > 0.5t_0$), we show a single experimental set for each size of macrodrop, rather than the mean over three repetitions of the experiment, as shown for microdrops. Arrows indicate increasing R_f. (*a*) Time evolution of the normalised droplet depth $H_b/2R_f$ for drops of $R_f = 38.6$ μm and 1.07, 1.77, 2.17, 2.82 mm. Time is normalised by the total experimental duration t_0. Inset: comparison between r_c and H_b for each drop. Dotted lines are least-square fits of a linear function. (*b*) Time evolution of normalised cap radius r_c for macrodrops ($R_f > 1$ mm) and (inset) a microdroplet ($R_f = 38.6$ μm). The large star on the horizontal axis of the inset figure indicates t_0 for the microdroplet. Target symbols on the macrodrop data correspond to $t = t_m$, the time at which the measured buoyant force is a maximum (see figure 10*a*).

figure 9*b*) was identified by the sudden fading of this bright spot, which was verified to coincide with detachment through observations of side view images.

The inset of figure 9(*a*) shows r_c/R_f plotted against $H_b/2R_f$ for each of the droplets; least-square fits of the form $H_b/2R_f = Ar_c/R_f + B$, shown as dotted lines, suggest H_b is linearly related to r_c at all times. Therefore, while we cannot directly image the apparent contact line for the microdroplet for $t \gtrsim t_0/2$, the continuous slowing of sinking up to t_0 (figure 9*a*) suggests a continuous slowing of spreading dynamics (figure 9*b*) as well. We note that as R_f is increased, the gradient (A) increases from around 1/10 for microdroplets to an almost constant value of ∼1/2 for the largest macrodroplets studied.

Reducing the drop size, or R_f, reduces the Bond number $Bo = (\rho_d - \rho_o)gR_f^2/\gamma_{oa}$, a commonly used measure of the relative strength of gravitational versus capillary stresses. This is reflected in the sinking dynamics shown in figure 9(*a*); an increase in R_f results in an overall downward shift in the normalised depth $H_b/2R_f$. Physically, this corresponds to larger droplets hanging further below the far-field oil level, an indication that the droplets' weight pulls down on the oil surface. In turn, the surface deforms in response to the net effect of the droplet weight and buoyancy, generating an opposing capillary force. For droplets with $R_f \leq 1.77$ mm (the top three curves in figure 9*a*), the curves overlap at $t \lesssim 0.4t_0$; the difference between droplet weights is therefore not strongly reflected in the relative deformation of the oil surface at the start of stage 3, a consequence of the dominant capillary stresses for small R_f (and Bo). However, the difference in R_f for the smallest droplets becomes apparent later in stage 3, visible as a divergence of the top three curves in figure 9(*a*). This is due to capillary forces diminishing as oil spreads over the drop, reducing the radius r_c of the apparent contact line, about which the capillary stresses are localised. The relative dominance of capillary and gravitational stresses is therefore dependent not only upon the size of the droplet (or Bo), but also on the extent of engulfment, due to the diminishing size of the contact line.

3.2.3. *Evolution of gravitational and capillary forces*

The total force with which the droplet pulls on the oil surface is determined by the net effect of the droplet weight $F_w = 4/3\pi R_f^3 \rho_d g$ plus the buoyant force F_b due to displaced oil, which act in opposite directions to one another. Consistent with previous studies of droplets suspended at interfaces (Phan *et al.* 2012, 2014), we estimate the instantaneous value of F_b by assuming it is equal to the weight of oil displaced within the regions V_1 and V_2 sketched in figure 8(*a*), such that

$$F_b = \rho_o g(V_1 + V_2). \tag{3.1}$$

The lower volume V_1 occupied by the droplet below the apparent contact line is closely approximated by a spherical cap of radius R_f and base radius r_c (see § 3.2.4), while the upper volume V_2 between the apparent contact line and the far-field oil level is a cylinder of height h_* and radius r_c. The weight of oil displaced in the meniscus outside the apparent contact line is then equivalent to the total capillary force acting at the apparent contact line (Keller 1998). Through side view images, we were able to measure h_*, the height at which the oil surface meets the droplet, and top view images provide measurements of r_c, which yield F_b/F_w through (3.1). We plot the quantity as a function of r_c/R_f in figure 10(*a*) for the two largest droplets studied ($R_f = 2.17$ and 2.82 mm). Since r_c decreases monotonically in time, this representation is equivalent to the time evolution of F_b/F_w. We consistently observe a non-monotonic variation in F_b/F_w over each experiment, with F_b/F_w reaching a maximum value (at a time $t_m < t_0$), before decreasing to a final value of $\rho_o/\rho_d \approx 0.971$ as the droplet detaches from the oil surface at $r_c = 0$ (equivalent to $t = t_0$). The maximum value of F_b/F_w for each data set is indicated by a target symbol. The corresponding point at $t = t_m$ is indicated in the same way for each macrodroplet in figure 9(*b*), showing that the maximum value of buoyancy approximately coincides with the inflection point of $r_c(t)$. We note that the non-monotonicity of F_b/F_w is due entirely to the contribution to buoyancy $F_{b2} = \rho_o g V_2$ (shown in the inset of figure 10*a*) due to the volume V_2 displaced by the droplet as it pulls down on the oil surface. By contrast, the contribution $F_{b1} = \rho_o g V_1$ (dashed line in figure 10*a*) due to the volume displaced below the apparent contact line depends only on r_c/R_f and increases monotonically as oil spreads to cover more of the droplet.

We can also estimate the instantaneous capillary force F_c acting upwards on the droplet by integrating the vertical component of air–oil surface tension around the apparent contact line, which yields

$$F_c = 2\pi r_c \gamma_{oa} \sin(\phi_a). \tag{3.2}$$

Here, ϕ_a is the apparent inclination of the oil surface relative to the horizontal, measured in the vicinity of the contact line, as indicated in the inset of figure 8(*a*). The angle is extracted from profiles like the ones shown in figure 8(*b*), by fitting fifth order polynomials to the points fitted to the oil–air surface and recording the inclination at the apparent point of inflection close to the contact line. The measured values of ϕ_a are plotted in figure 10(*b*). For clarity, we only show data for the two largest droplets studied. As shown in the inset of figure 10(*b*), where we have plotted ϕ_a as a function of the normalised buoyant force F_b/F_w, the slow initial increase in ϕ_a ($t \lesssim 0.6t_0$) coincides with the increase in F_b observed for the first part of the experiment. Here, the reduction in the capillary force due to the reduction in r_c associated with the advancing contact line is partially compensated for by an increase in F_b, and the surface inclination remains roughly constant. After F_b reaches a maximum and begins to wane, the increase in ϕ_a is far more pronounced for both drops (figure 10*b* inset), as the surface reacts to a decrease in both r_c and F_b.

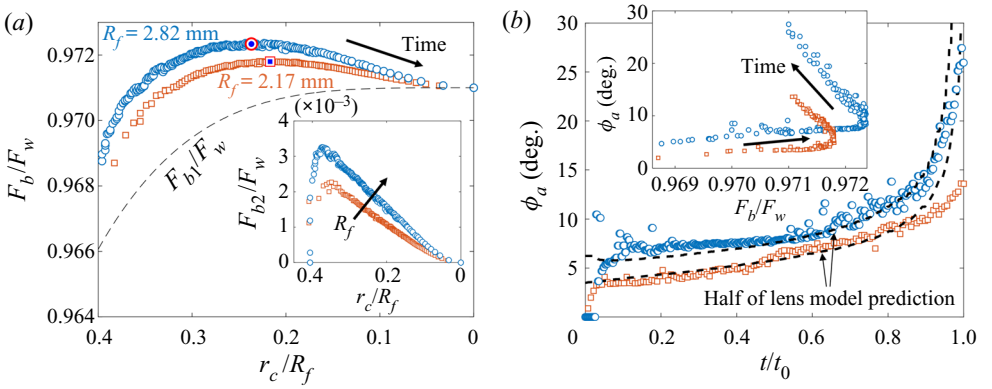

Figure 10. (*a*) Total buoyant force $F_b = F_{b1} + F_{b2}$ as a function of r_c/R_f for droplets of in-flight radii $R_f =$ 2.17 mm (squares) and 2.82 mm (circles) on 1000 cSt PDMS oil. Symbols are consistent with (*b*). Forces are normalised by the droplet weight F_w. The dashed line is F_{b1}, the contribution due to the oil displaced in volume V_1, which is shown in figure 8(*a*). The maximum values of F_b, determined from a fifth-order polynomial fit to the data, are indicated by target symbols. The arrow indicates increasing time. Inset: the contribution F_{b2} due to V_2 as a function of r_c/R_f. The arrow indicates increasing R_f. (*b*) Time evolution of the oil surface inclination ϕ_a for the same data as shown in (*a*). Dashed lines are half the value ϕ_a^{lens} predicted for a liquid lens. Inset: comparing the evolution of ϕ_a and F_b/F_w for the same two drops.

The surface therefore seems to deform in response to variations in both the effective weight of the drop and the geometry of the apparent contact line.

Since we are able to estimate both F_c and F_b, we may examine this observation more closely by comparing the instantaneous configuration of the system to the analogous liquid lens equilibrium state of partially wetting droplets (i.e. water on vegetable oil; Phan *et al.* 2012, 2014); in the latter case, $F_c = F_w - F_b$, i.e. the surface around the droplet deforms to exactly oppose the effective weight of the droplet. From (3.1) and 3.2 we can therefore calculate the inclination ϕ_a^{lens} for a liquid lens at equilibrium

$$\phi_a^{lens} = \arcsin\left(\frac{F_w - F_b}{2\pi r_c \gamma_{oa}}\right). \tag{3.3}$$

Equation (3.3) is an overestimate as it assumes the droplet's effective weight is opposed by capillarity only and ignores viscous stresses. However, the qualitative behaviour is close to what we observe in experiments and in fact the quantitative agreement is very good for $\phi_a^{lens}/2$, as shown by the dashed lines in figure 10(*b*); these lines were calculated from (3.3) using experimental values of $r_c(t)$ and $F_b(t)$ for each drop. By halving the predicted value ϕ_a^{lens}, we are able to achieve strong agreement with experimental values of ϕ_a over the majority of each experiment. The qualitative agreement suggests that the surface deforms in such a way as to provide a reaction force to the effective weight $F_w - F_b$ of the droplet, responding to variations in both F_b and r_c.

Since the predicted value ϕ_a^{lens} is around half the experimental value ϕ_a, this suggests that only half of the effective weight is accounted for by capillarity. As the system obeys Stokes flow ($Re \ll 1$) there must be a net force balance at all times, with the remaining instantaneous upwards force on the droplet due to viscous resistance. The observation that viscous forces are, throughout stage 3, approximately equal in magnitude to capillary forces acting on the droplet may reflect the presence of flows in the oil phase driven by gradients in capillary stresses along the deformed oil surface. We are, however, unable to comment on the specifics of any such flows, although by dusting the oil surface with

microscopic polymer beads to act as tracer particles prior to depositing droplets, we were able to observe flows driven radially inwards along the oil surface towards the droplet, which recirculated downwards along the droplet surface close to the apparent contact line. While these experiments hint at the existence of complex recirculation flows within the peeling region, we are unable to present a detailed study of such flows due to the sensitivity of interfacial mechanics to particle perturbations. Instead, we will proceed in the following section to examine the peeling flow around the apparent contact line, for which we have sufficient experimental evidence.

3.2.4. *Peeling dynamics at the advancing contact line*

The spreading of oil over the droplet cap during stage 3 is analogous to classical spreading or peeling phenomena (Bonn *et al.* 2009; Lister *et al.* 2013), with the cloaking layer acting as a precursor film. As such, variations in curvature local to the apparent contact line drive a peeling flow. Hence, by studying how surface deformations respond to either changing the size of the droplet or the evolving geometry around the apparent contact line, we can rationalise many of the dynamical features of engulfment discussed in § 3.2.2. The extent of surface deformations at any instant may be inferred largely from the apparent contact angle θ_c and the radius r_c of the apparent contact line (see figure 8*a*). It should be noted that as the droplet is engulfed and r_c tends to zero, variations in r_c will become increasingly important; however, consistent with previous studies of peeling flows, we find that much of the observed variations in engulfment dynamics (both over time and for different size drops; see figure 9) may be interpreted through considering only the evolution of the apparent contact angle $\theta_c = \phi_a + \phi_b$ (see inset of figure 8*a*).

Figure 11 shows the time evolution of θ_c, ϕ_a and ϕ_b (see labels) for the two largest droplet sizes studied. The first component, ϕ_a, has already been discussed and indicates deformation of the oil surface in response to the droplet's effective weight. It is therefore dependent on the size of the droplet (more specifically, the Bond number Bo), as well as the relative size of the apparent contact line, r_c/R_f. To illustrate this, we recall that $\phi_a \approx \phi_a^{lens}/2$ (an experimental observation; see (3.3)). Due to the cloaking layer, the droplet is completely submerged during stage 3, and $F_b \approx 4/3\pi R_f^3 \rho_o g$. We therefore have

$$\phi_a \approx \frac{1}{2} \arcsin\left(\frac{2Bo}{3r_c/R_f}\right). \tag{3.4}$$

While (3.4) neglects the subtle evolution of F_b (see § 3.2.3), it nonetheless captures the essential dependence of surface deformations on the size of the droplet, as well as the monotonic increase in ϕ_a over stage 3 as r_c decreases (figure 11).

The second component ϕ_b, meanwhile, decreases monotonically due to geometric constraints; as the contact line moves inwards, towards the apex of the drop, ϕ_b must reduce as the local surface of the droplet becomes increasingly level. The portions of the droplet surface above and below the contact line are described (in the absence of gravity) by spherical caps (Phan *et al.* 2014). Because almost all of the droplet in stage 3 is below the contact line, we would expect the lower portion of the droplet to approximate a spherical cap of radius R_f and base radius r_c. In this case, $\phi_b(r_c) = \arcsin(r_c/R_f)$, and hence ϕ_b tends to zero at $t = t_0$ (and $r_c = 0$). However, in practice our droplets hang from the surface in a deformed pendant shape due to their weight stretching them vertically. This results in a constant offset angle ϕ_{b0} such that

$$\phi_b = \arcsin(r_c/R_f) + \phi_{b0}, \tag{3.5}$$

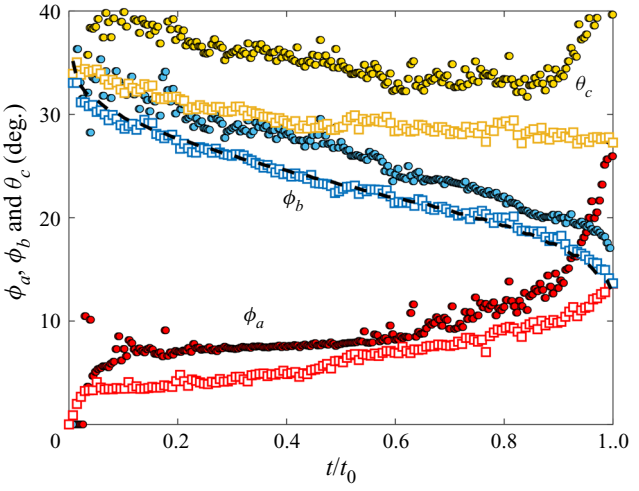

Figure 11. Time evolution of ϕ_a and ϕ_b (red and blue points) and the apparent contact angle $\theta_c = \phi_a + \phi_b$ (yellow points) for the same data shown in figure 10. Circles and squares are data points corresponding to droplets with $R_f = 2.82$ mm and $R_f = 2.17$ mm, respectively. The dashed line is (3.5), plotted with experimental data for the smaller droplet, with $\phi_{b0} = 13.1^\circ$.

as shown in figure 11 where we have plotted (3.5) (dashed line) for the smaller droplet; here, choosing $\phi_{b0} = 13.1^\circ$ produces the best fit to the data. The offset ϕ_{b0} decreases for smaller droplets (lower Bo) as capillary stresses become dominant over gravitational effects and the droplet shape becomes increasingly spherical.

We can empirically approximate θ_c using (3.4) and (3.5), which gives

$$\theta_c \approx \frac{1}{2}\arcsin\left(\frac{2Bo}{3r_c/R_f}\right) + \phi_{b0} + \arcsin\left(\frac{r_c}{R_f}\right). \tag{3.6}$$

The first and second terms on the right-hand side enhance spreading, in the sense that they yield increasing deformations (larger θ_c) for larger droplets or as the apparent contact line advances (r_c reduces). Both of these terms depend directly on the size of the droplet (or Bo). The third term, meanwhile, suppresses spreading (deformations reduce with r_c) and depends only on the geometry of the contact line, through r_c/R_f. The inflection of $r_c(t)$ observed for macrodroplets (figure 9*b*) is therefore due to a competition between the first and third terms, which are associated with ϕ_a and ϕ_b, respectively. The initial slow increase in ϕ_a is outpaced by the (purely geometric) reduction in ϕ_b, resulting in weaker deformations and slowing engulfment. Later, the rapid increase in ϕ_a in response to the waning capillary and buoyant forces (see figure 10*b*) corresponds to faster engulfment.

The contrasting engulfment dynamics observed for microdroplets (i.e. no inflection of $r_c(t)$ or $H_b(t)$; see figure 9) may also be interpreted within this framework. Since $Bo \ll 1$, microdroplets are almost perfectly spherical and $\phi_{b0} \approx 0$. Moreover, if $Bo \ll r_c/R_f$ then from (3.4) and (3.6) we expect $\phi_a \approx 0$ (the surface hardly deflects) and $\theta_c \approx \arcsin(r_c/R_f)$; hence, deformations will diminish over time and engulfment will slow continuously as r_c reduces. The final detachment of the droplet and oil surfaces is nonetheless due to gravity-driven deformations, consistent with the predicted increase in ϕ_a for $r_c/R_f \lesssim Bo$ (3.6). For microdroplets ($Bo \ll 1$) this must occur so close to detachment that we cannot observe it in practice. However, this argument demonstrates that gravity is central to the engulfment process for any size of droplet because r_c/R_f will always tend to zero (and therefore become $< Bo$) due to peeling.

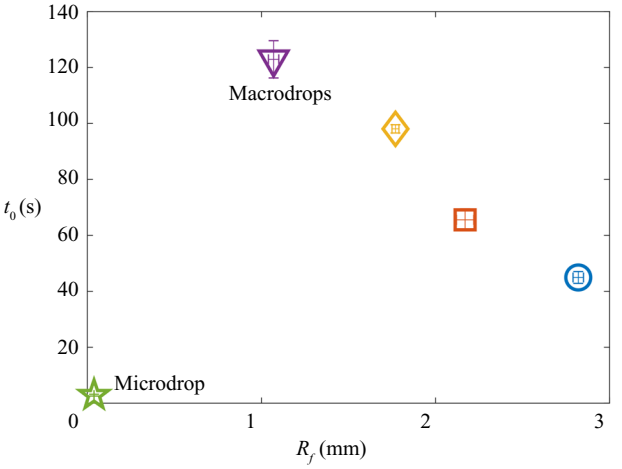

Figure 12. Total experimental duration t_0 for each R_f studied. Vertical error bars are the standard deviations of at least three repetitions of the experiments.

We note that for peeling flows, the apparent contact angle generally dictates the velocity of the peeling front (i.e. the contact line; see Ducloué *et al.* 2017). However, θ_c remains approximately constant for the smaller of the two droplets represented in figure 11 for $t \gtrsim 0.6t_0$, while at the same time the rate of engulfment increases. This suggests that the speed of the apparent contact line is not strongly dependent on variations in θ_c late in stage 3, at least for the smaller droplet. As already noted, to gain a fuller picture of the peeling flow one would need to consider surface deformations not captured by θ_c alone, which is beyond the scope of this study. The analysis presented in this section nonetheless illustrates the basic driving mechanisms of the flow; that is, gravitational forces and geometric constraints.

3.2.5. *Effect of droplet size on engulfment time*

Figure 12 shows the relation between droplet size R_f and engulfment time t_0. The maximum t_0 occurs for the smallest macrodrops with $R_f = 1.07$ mm. Increasing R_f for macrodrops then results in faster engulfment (lower t_0), while the microdrop with $R_f = 38.6$ μm is engulfed much faster than any of the macrodrops. This non-monotonic trend reflects two competing effects of increasing the droplet size. At high *Bo* (macrodrops), larger droplets generate greater deformations in the oil surface, which drives faster engulfment, as already discussed. At very low *Bo*, however, such gravitational effects are negligible, and increasing the size of the droplet predominantly acts to increase the area of the droplet over which oil must spread. Hence, for microdrops we expect slower engulfment for increasing R_f. In agreement with figure 12, this result also implies that there is a critical value of R_f at which the time taken to engulf a droplet reaches a maximum.

3.2.6. *Effect of oil viscosity*

The time evolution of the cap radius r_c on oils of different kinematic viscosity ν is shown in figures 13(*a*) and 13(*b*) for microdroplets with $R_f = 38.6$ μm and macrodroplets with $R_f = 1.07$ mm, respectively. For these experiments, we used PDMS oils of viscosities $\nu = 100$, 1000, 30 000 and 100 000 cSt. The main effect of increasing ν is to slow the engulfment of the droplet, as expected, which is reflected in an increase in the experimental duration t_0. We note that macrodroplets deposited onto 100 cSt oil (blue circles in

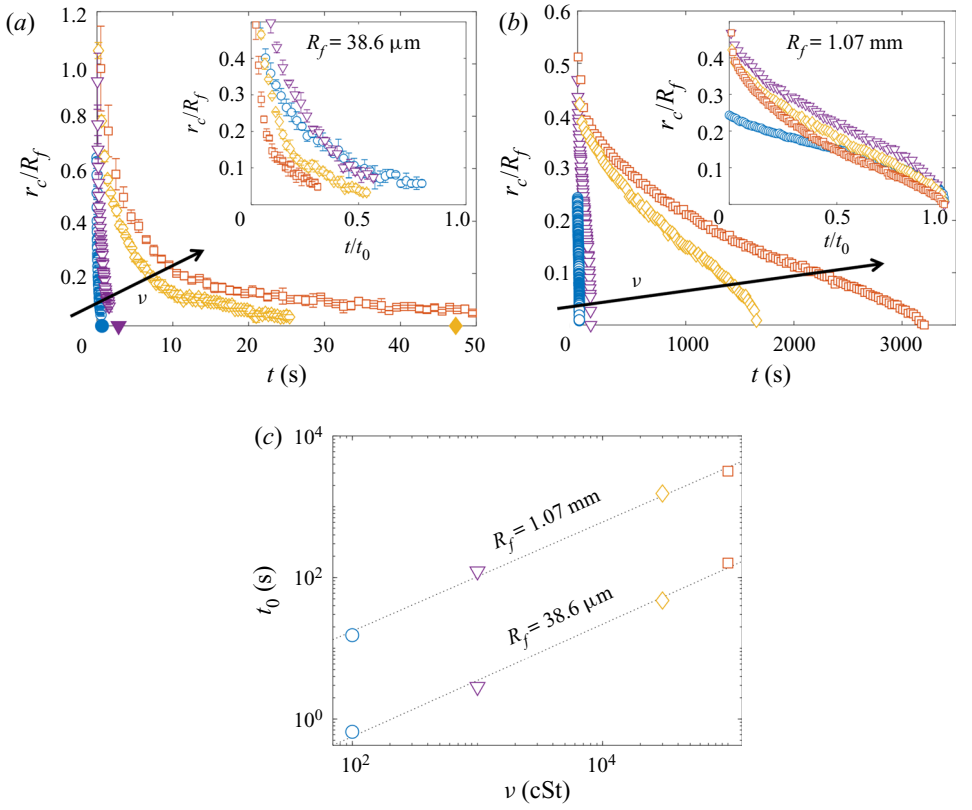

Figure 13. The effect of oil viscosity ν. Panels (*a*,*b*) show the time evolution of the normalised apparent contact line radius r_c/R_f for (*a*) microdrops with $R_f = 38.6$ μm and (*b*) macrodrops with $R_f = 1.07$ mm deposited on oils of viscosities $\nu = 100$, 1000, 30 000 and 100 000 cSt. Arrows indicate increasing ν. The insets show the same data with time normalised by the experimental duration t_0. Solid symbols in (*a*) indicate t_0 for each experiment; data at t_0 are not plotted for the highest ν experiment, for the sake of clarity. Panel (*c*) shows t_0 as a function of ν for the data in (*a*,*b*). Dotted lines are least-square fits of the form $t_0 \sim \nu^{\alpha}$, where $0.77 \leq \alpha \leq 0.8$.

figure 13*a*,*b*) show distinct dynamics compared with the other (larger) viscosities; most notably, the normalised cap radius r_c/R_f is significantly lower at early times $t < 0.5t_0$ (see inset of figure 13*b*). This may reflect the fact that $\nu = 100$ cSt is around the threshold value $\nu_{threshold}$ at which we expect the initial conditions of stage 3 to be significantly affected by inertia–capillary effects (see figure 15 in Appendix B). For all ν tested, the dynamics of engulfment for macro- and microdrops is qualitatively similar to that described in the previous section for drops on 1000 cSt oil. The insets of figures 13(*a*) and 13(*b*) show the same data with time normalised by t_0, to allow for qualitative comparison of the data at different ν.

In figure 13(*c*), the total experimental duration t_0 is plotted against ν for each of the drop sizes. The dashed lines are least-squares fits of the form $t_0 \sim \nu^{\alpha}$ (note the logarithmic scales). For $R_f = 38.6$ μm and 1.07 mm, we find similar values of $\alpha = 0.77$ and 0.80, respectively. Hence, doubling the oil viscosity results in the droplet being engulfed in somewhat less than double the time. Compare this to our observations of stage 2 (see § 3.1), for which the time scale $\tau_\gamma = \mu R_f/\gamma_{oa}$ scales linearly with oil viscosity; the nonlinear scaling ($\alpha \neq 1$) of stage 3 suggests that the effect of ν is not simply to oppose bulk displacement of the oil phase. We speculate that these effects originate in the cloaking

layer of oil covering the droplet. At equilibrium, the thickness of the cloaking layer would be determined by a balance between disjoining pressure and capillary pressure in the film, neither of which should depend strongly on oil viscosity. However, the dynamical spreading process which forms the cloak may well result in an initial film thickness which depends on ν, as is generally the case for coating flows (Landau & Levich 1942; Bretherton 1961). The cloaking layer acts as a precursor film as oil spreads to cover the droplet in stage 3; hence, variations in the thickness of the film could modify the time scale of engulfment.

4. Conclusion

We have studied the engulfment of an aqueous droplet deposited on a deep layer of oil which wets the droplet perfectly. Our study focuses on the evolution of the droplet and the oil surface from the instant they first make contact until the instant they detach. We have identified two key stages in this evolution: an earlier stage (stage 2), driven by capillarity and opposed by bulk viscous stresses in the oil, during which the droplet is rapidly pulled beneath the level of the oil surface; and a subsequent stage (stage 3) driven by a coupling between gravity and capillarity as the system slowly evolves towards the instant when the droplet detaches from the oil surface and sinks. Our study of stage 3 in particular revealed several unexpected features of engulfment. By comparing our unstable but slowly evolving system with a stable liquid lens in § 3.2.3, we showed that the viscous and capillary forces acting instantaneously on the droplet over much of stage 3 contribute equally to oppose the weight of the droplet. We then studied the gradual spreading of the apparent contact line in stage 3 as a peeling flow. We found that the opposing effects of geometry and gravity resulted in a maximum engulfment time t_0 for droplets of intermediate size (around 1 mm in radius).

By contrast with studies of droplets penetrating immiscible liquid layers due to impact conditions (Wang *et al.* 2020), the dynamics of engulfment as presented here is entirely independent of impact (see Appendix A), driven instead by unsteadily evolving gravitational and capillary forces, with oil viscosity having a non-trivial effect on the time scale of engulfment (see § 3.2.6). A key feature of the system in determining this complex dynamics is the presence of the cloaking layer of oil over the droplet formed early in stage 2. To our knowledge, only one previous study has examined the dynamical formation of cloaking layers (Sanjay *et al.* 2019). Our work continues the story, demonstrating that the subsequent peeling of the cloaking layer from the droplet surface is itself a remarkably complex and subtle process.

Our study of individual droplets has implications for more complicated, coupled systems. During stage 3, for instance, the droplet remains transiently suspended at the oil–air interface for time scales ranging from tenths of a second to an hour, depending on the droplet size and oil viscosity. The instantaneous configuration of the system over this stage is reminiscent of partially wetting droplets or even rigid particles suspended at an interface at equilibrium. This naturally raises questions of how our droplets may behave in the context of self-organising systems, such as particle rafts or soft crystals. For instance, two particles both denser than the underlying fluid layer will tend to pull the fluid surface down at the pinned contact line and may therefore attract one another due to capillary stresses acting to minimise the curved fluid interface between the two (Vella & Mahadevan 2005). On the other hand, if one of the particles is less dense than the fluid and floats (pulling the surface up), the particles will repel due to the inflected surface between them. While we would expect the same buoyant–capillary interactions between our droplets, the constant spreading of oil to cover the drops must also drive flows within the oil phase, absent in interfacial systems studied previously. These time-dependent flows

may conceivably enhance or oppose the buoyant–capillary interactions between droplets and particles of different densities, and their exact influence on self-organisation is difficult to predict. Moreover, it remains to be seen how a rigid particle, perfectly wetted by a fluid substrate, may behave.

As a final remark, we note that the high-viscosity regime ($Oh \gtrsim 1$) we chose to examine is broadly relevant to oil spills, since many of the planet's natural oil reserves have kinematic viscosities of hundreds of cSt or more (Fingas & Fieldhouse 2012). In addition, the viscosity of crude oil slicks tends to increase over time as volatile fractions evaporate. The interaction of oil slicks with droplets is then central to a number of important practical applications. Spraying oil spills with droplet dispersants, for instance, is a routine method intended to enhance microbial oil degradation by increasing the oil–water interfacial area. While the efficacy of doing so remains contentious (Kleidienst *et al.* 2015), the practice is used globally and on massive scales, such as in the 2010 Deepwater Horizon oil well blowout in the Gulf of Mexico. We note that dispersants often constitute a complex mixture of polymers and surfactants. A preliminary study suggested that significant contamination from surfactant may prevent the formation of a cloaking layer, halting the engulfment process and stabilising the droplet as a lens at the oil surface (compare with Phan *et al.* (2014), see § 1). However, provided the cloak can form (a question beyond the scope of this study), our analyses of early-time submersion (§ 3.1.2) and peeling dynamics (§ 3.2.4) suggest that the droplet should ultimately be engulfed regardless of variations in surface tension due to surfactants. Moreover, our study of PEDOT:PSS (§ 3.1.2), which is a complex fluid, suggests that at the low shear rates present in engulfment flows, the presence of polymers does not necessarily modify the dynamics. Hence, our fundamental study of engulfment has relevance to a much broader class of problems.

Acknowledgements. We thank M. Quinn for his technical support. We also thank A. Hazel and D. Vella for helpful discussions of an earlier version of the manuscript.

Funding. CC was funded by an EPSRC DTP studentship, AJ and ABT by EPSRC grant EP/P026044/1 and DPP by EPSRC grant EP/R045364/1.

Declaration of interests. The authors report no conflict of interest.

Author ORCIDs.
Callum Cuttle https://orcid.org/0000-0002-1852-5599;
Alice B. Thompson https://orcid.org/0000-0001-9558-1554;
Draga Pihler-Puzović http://orcid.org/0000-0002-7458-100X;
Anne Juel https://orcid.org/0000-0003-3342-7388.

Appendix A. Effect of impact velocity on early-time engulfment

Figure 14 shows the result of impacting droplets of $R_f = 1.07$ mm at different impact velocities $13 \leq U_f \leq 50$ cm s^{-1}. We varied U_f by changing the height from which the droplets fell before impacting the oil layer. The inset of figure 6(*d*) shows the lifetime T_{AC} of the air cushion as a function of U_f. We consider the air cushion to be formed after the droplet's final bounce following impact, and so we identify the start of T_{AC} by the last frame in which the lower surface of the droplet is visible above the oil crater. The value of T_{AC} increases monotonically with impact velocity, particularly over the range $31 \leq U_f \leq 50$ cm s^{-1}, varying only slightly for $13 \leq U_f \leq 31$ cm s^{-1}. For $13 \leq U_f \leq 31$ cm s^{-1}, $T_{AC} \approx 0.1$ s, similar to the time scale over which impact-generated capillary waves persist on the droplet's surface after impact. Hence, over this range of U_f, some small amplitude droplet oscillations are still visible when the air cushion ruptures (see figure 6*b*).

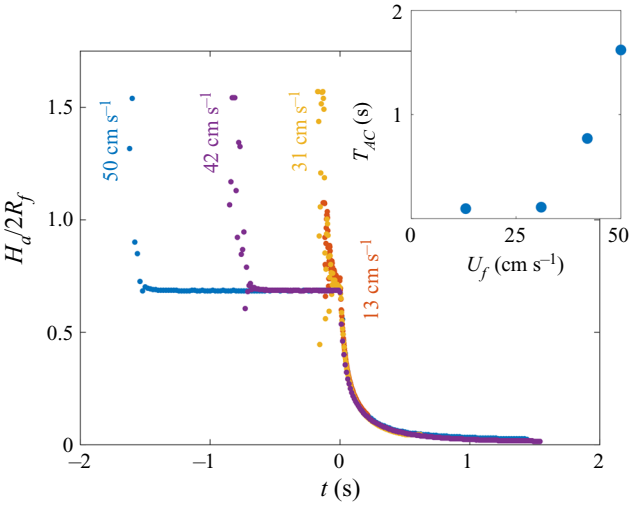

Figure 14. Time evolution of the normalised height $H_a/2R_f$ of the droplet cap above the oil surface (see figure 6) for four impact velocities $13 \leq U_f \leq 50$ cm s^{-1}. Inset: lifetime T_{AC} of the air cushion as a function of U_f.

At the end of stage 1 ($t = 0$), all droplets sit at around the same height, $H_a/2R_f \approx 0.7$, relative to the far-field oil level. This configuration is similar to the equilibrium lens state calculated numerically by Wong, Adda-Bedia & Vella (2017) for a perfectly non-wetting droplet on a liquid layer. By analogy, the presence of the air cushion in our experiments acts to make the droplet effectively non-wetting on the oil, and the state of the system at the end of stage 1 corresponds to an approximate balance between capillary stresses due to the deformed oil surface and the droplet's weight. The dynamics of stage 2 all fall onto the same curve for $H_a(t > 0)$ to within experimental variability ($t > 0$ in figure 6*b*). In fact, repeated tests indicate that variations in U_f did not measurably affect the dynamics of engulfment after $t = 0$, for either macro- or microdroplets.

Appendix B. Effect of substrate viscosity on the time scales of engulfment

We conducted experiments over a broad range of oil viscosities, $20 \leq \nu \leq 10^5$ cSt. Figures 15(*a*) and 15(*b*) compare the engulfment of droplets with $R_f = 1.07$ mm deposited on 20 and 100 cSt oil baths, respectively. Side view images illustrate the 4 stages of engulfment introduced in figure 3. Stages 1 and 2 occur over comparable time scales for both viscosities; in both cases the air cushion ruptures at $t = 0$, leaving behind small air bubbles, and the droplet is pulled downwards as oil spreads over the droplet. However, the time scale associated with stage 3, as well as the qualitative droplet behaviours, differ significantly for 20 and 100 cSt oils. At the start of stage 2, the sudden onset of engulfment generates inertia–capillary waves which significantly distort the droplet surface (see § 3.1). Theses waves are dissipated by viscous resistance primarily within the oil phase. For the drops on 20 cSt oil, inertia–capillary waves persist on the droplet–oil surface throughout engulfment, evident in the vertically stretched shape of the droplet during stage 3 (figure 15*a*, $t = 0.02$ s). By contrast, droplets on oils of $\nu \geq 100$ cSt (figure 15*b*, $t = 0.16$ s) show no clear evidence of the influence of inertia–capillary waves, with the droplets gradually descending below the oil surface. The drop encapsulated in 20 cSt oil detaches from the surface over a time scale comparable to that of stage 2

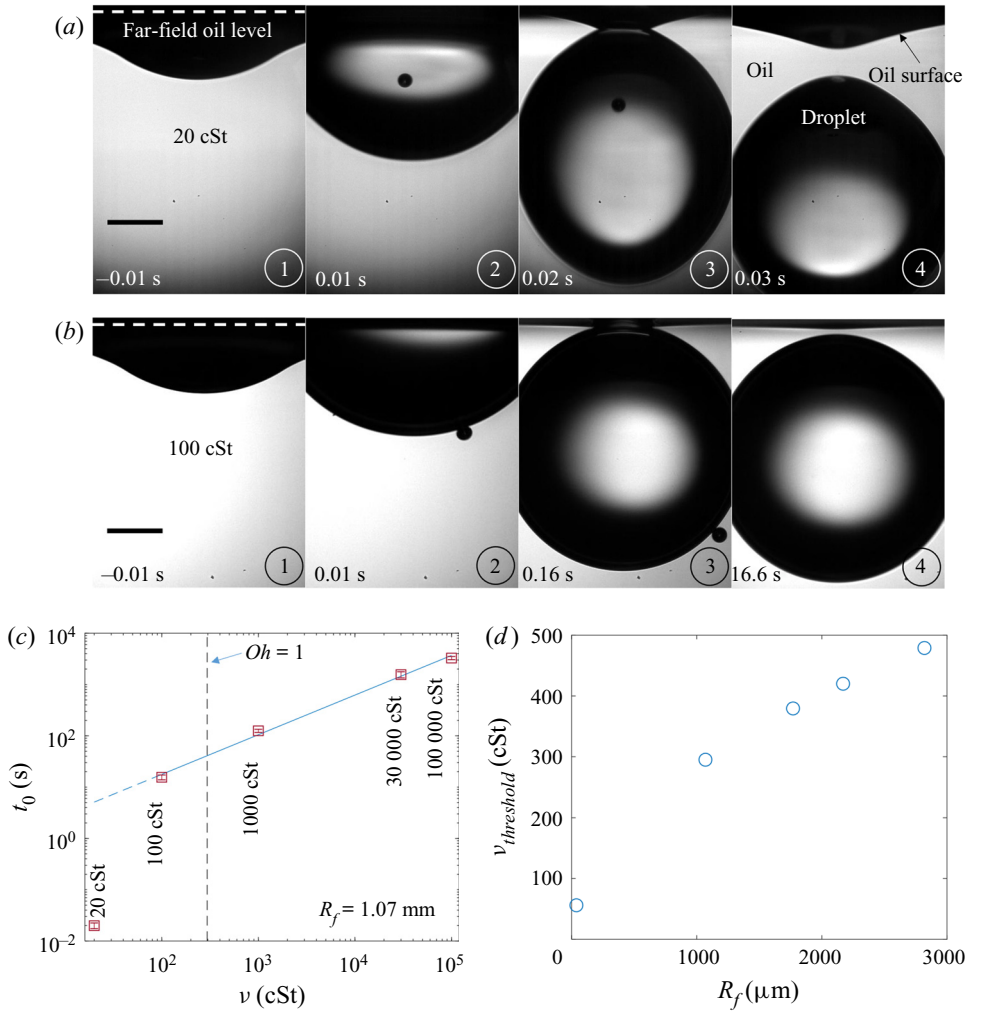

Figure 15. Effect of oil viscosity on time scales of engulfment. (*a*,*b*) Side view time series for droplets with $R_f = 1.07$ mm deposited on 20 and 100 cSt oils, respectively. The droplet and oil phases are labelled, as is the far-field level of the oil surface, away from the perturbed region around the droplet. Light is refracted at the curved oil and droplet surfaces, reducing the intensity of light transmitted to the camera objective. Hence, the droplet–air interface is not visible through the oil surface, and the droplet appears brightest within a central region. The times indicated are measured relative to the rupture of the air cushion. The stages of engulfment (1–4; see § 1) are indicated in the bottom right corner of each image. Scale bars are 0.5 mm. (*c*) The time t_0 at which the droplet detaches from the oil surface as a function of oil kinematic viscosity ν for drops with $R_f = 1.07$ mm. The fitted curve (note the log–log scale) corresponds to a power law $t_0 \sim \nu^{0.8}$ for $\nu \geq 100$ cSt data. Error bars (which are smaller than the symbols) are standard deviations over at least three repetitions of the experiment. (*d*) Threshold oil viscosity $\nu_{threshold}$ for each drop size R_f investigated, estimated from setting the Ohnesorge number $Oh = 1$ (defined in the main text). The corresponding value for $R_f = 1.07$ mm is indicated by a dashed line in (*c*).

(∼0.03 s), while the drop on 100 cSt oil remains suspended below the oil surface for a relatively long time (∼16 s) compared with the preceding stage, before finally detaching and sinking. The contrasting time scales of the two processes are highlighted in figure 15(*c*), which shows the time of detachment t_0 as a function of ν for droplets with $R_f = 1.07$ mm. At $\nu \geq 100$ cSt, t_0 appears to vary with viscosity as $t_0 \sim \nu^{0.8}$ (see § 3.2.6),

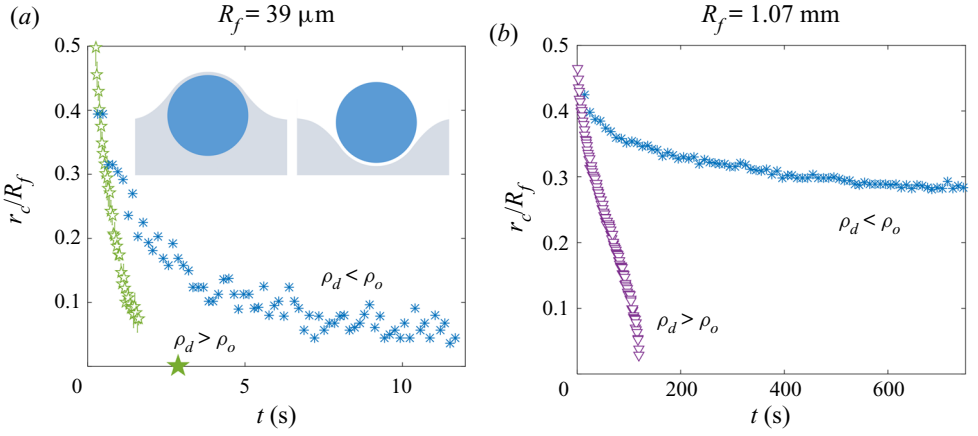

Figure 16. Time evolution of the apparent contact line radii r_c for (*a*) micro- and (*b*) macrodrops on different 1000 cSt oils, with $R_f = 38.6$ μm and 1.07 mm, respectively. Blue stars are data points for droplets deposited on PPMS oil, with density ρ_o slightly greater than the density of water, ρ_d. Pentagrams and triangles are data for drops on PDMS oil ($\rho_o < \rho_d$), consistent with figure 9. The inset of (*a*) shows schematic diagrams of (left) a cloaked droplet at rest, floating on PPMS oil and (right) a droplet transiently at rest on a draining film of air.

as indicated by the power law fit (note the log–log scale). The point at 20 cSt, however, deviates from this power law by two orders of magnitude, suggesting the influence of inertia–capillary waves at low ν may significantly modify the dynamics of engulfment. We choose to focus our investigation on the high-viscosity regime. To formalise this statement, we define the Ohnesorge number $Oh = \rho_o \nu/\sqrt{2R_f \rho_o \gamma_{do}}$, where ρ_o and γ_{do} refer to the oil density and droplet–oil interfacial tension, respectively. We have chosen the in-flight diameter of the drop as the length scale. Oh quantifies the ratio between the typical period of oscillation associated with inertia–capillary waves on the droplet–oil interface and the time scale of viscous damping of inertial stresses in the oil phase ($\sqrt{(2R_f)^3 \rho_o/\gamma_{do}}$ and $(2R_f)^2/\nu$, respectively). We define our threshold ν as that which satisfies $Oh \gtrsim 1$, that is $\nu_{threshold} \approx \sqrt{2R_f \gamma_{do}/\rho_o}$. This corresponds to a situation wherein inertia–capillary waves are dissipated over time scales comparable to or less than a single period of oscillation, and should therefore not significantly affect the dynamics of engulfment. Figure 15(*d*) shows $\nu_{threshold}$ as a function of drop size R_f for the values studied, indicating a typical order of magnitude of hundreds of cSt.

Appendix C. Effect of droplet and substrate relative densities on engulfment

We also performed experiments with 1000 cSt PPMS oil, which has a density slightly greater than that of water (see table 1). The resulting time evolutions of r_c for a microdrop ($R_f = 38.6$ μm) and a macrodrop ($R_f = 1.07$ mm) are shown in figure 16(*a*,*b*) (blue stars). For comparison, we have plotted data for the same size drops on 1000 cSt PDMS oil on the same axes. For both of the drops on PPMS oil ($\rho_o > \rho_d$), we observe significantly slower spreading than for the corresponding drops on PDMS oil ($\rho_o < \rho_d$). The divergence of the data sets is most pronounced for the macrodroplets, which serves to highlight the dominant role of buoyant effects at larger R_f, or Bo. Since the droplets on PPMS oil did not sink, there was no identifiable instant of detachment. In addition, we did not observe any evidence of the apparent contact line closing, as is typically visible for macrodroplets

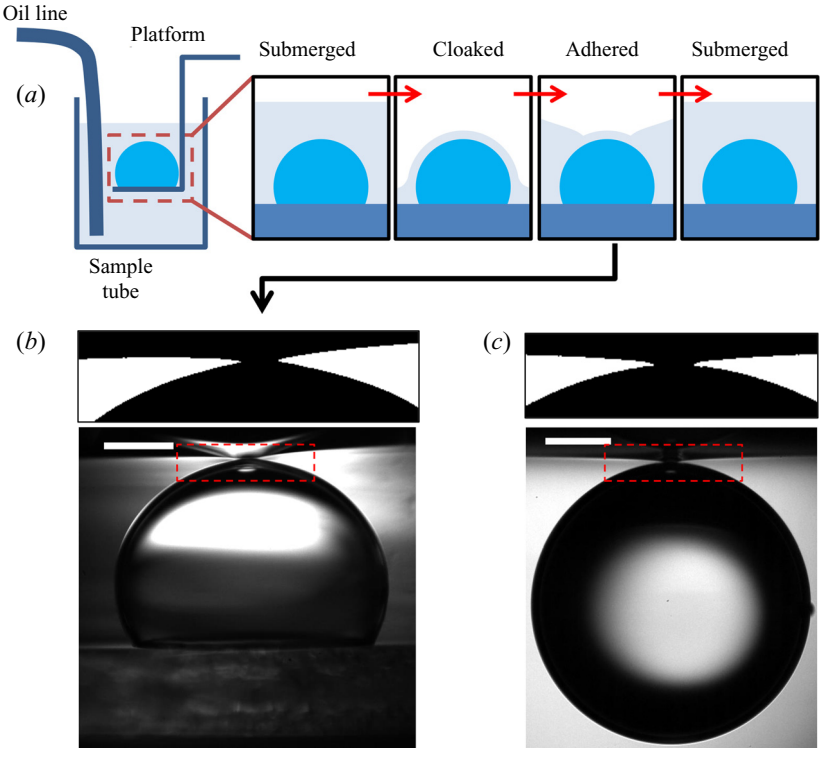

Figure 17. Oil surface adhesion for oil-cloaked droplets. (*a*) Experimental set-up and procedure. (*b*,*c*) Side view comparison of (*b*) an oil-cloaked droplet during the flooding of the sample tube and (*c*) a droplet during stage 3 of engulfment. Panel (*a*) shows enlarged views of the regions in the dashed boxes, where the oil–air and droplet–oil surfaces meet. The images have been binarised so that the oil phase appears white. Scale bars are 0.5 mm. The asymmetry of the oil surface profile in (*b*) is caused by meniscus effects due to the proximity of the droplet to the sample tube walls. This effect is absent in the much larger Perspex boxes used for (*c*). Oils of kinematic viscosity 100 cSt were used in both cases.

on PDMS oil. Instead, the contact line became increasingly faint, with r_c appearing to tend to a constant value, as inferred from the continuously decreasing gradient of the data in figure 16(*b*). This suggests that the system is tending towards an equilibrium state, sketched in the inset of figure 16(*a*), in which the droplet is cloaked, floating at the surface of the oil. In this configuration, buoyant forces on the droplet are balanced by the drop's weight and capillary stresses in the cloaking layer (distinct from the capillary stresses localised to a contact line for partially wetting liquid lenses). This is comparable to the situation at the end of stage 1, also sketched in the inset, when the droplet rests on a cushion of air. While the air film ultimately ruptures, the oil cloak in stable due to the effects of disjoining pressure (Schellenberger *et al.* 2015).

Appendix D. Adhesion of droplet and oil surfaces in the presence of a cloaking layer

To investigate the adhesion observed between droplets and the oil surface during engulfment, we performed a set of experiments shown schematically in figure 17(*a*). A water droplet with $R_f = 1$ mm was deposited onto a Perspex platform suspended by a cantilever. The droplet was lowered into a quartz sample tube (inner diameter 24 mm). The tube was partially filled with 100 cSt PDMS oil, the level of which could be adjusted

via a length of rubber tubing lowered into the tube, connected to a glass syringe mounted in a syringe pump (RS-232, KD Scientific). We initially flooded the tube, submerging the droplet entirely (see figure 17*a*). We then drained the oil to the level of the platform. This leaves the droplet coated in a cloaking layer of oil, which is stable since $S > 0$ (Schellenberger *et al.* 2015). After waiting one minute to allow the oil to settle, we submerge the droplet once again by pumping in oil at a fixed volumetric flow rate of $Q = 10.0\ \mathrm{ml\ min^{-1}}$. During this second stage of flooding, the oil surface rises more slowly in the vicinity of the cloaked cap, compared with the surrounding bath, suggesting an adhesive force between the droplet and oil surfaces. This is evident in the shape of the oil surface just before the droplet is entirely submerged, as shown in side view in figure 17(*b*). The upper image shows an enlarged view of the region around the cap of the droplet (red dashed line in the lower image), which has been binarised to emphasise the shape of the droplet and oil surfaces. For comparison, figure 17(*c*) shows images for a droplet with $R_f = 1.07$ mm deposited onto a deep bath of 100 cSt oil. The deformation of the oil surface in each experiment is strikingly similar, suggesting both are cloaked.

References

Anand, S., Rykaczewski, K., Subramanyam, S.B., Beysens, D. & Varanasi, K.K. 2015 How droplets nucleate and grow on liquids and liquid impregnated surfaces. *Soft Matt.* **11** (1), 69–80.

Bergeron, V. & Langevin, D. 1996 Monolayer spreading of polydimethylsiloxane oil on surfactant solutions. *Phys. Rev. Lett.* **76**, 3152–3155.

Berthier, J. & Brakke, K. 2012 *The Physics of Microdroplets*. Scrivener Publishing.

Bonn, D., Eggers, J., Indekeu, J., Meunier, J. & Rolley, E. 2009 Wetting and spreading. *Rev. Mod. Phys.* **81**, 739–805.

Brenner, H. 1962 Effect of finite boundaries on the Stokes resistance of an arbitrary particle. *J. Fluid Mech.* **12** (1), 35–48.

Bretherton, F.P. 1961 The motion of long bubbles in tubes. *J. Fluid Mech.* **10**, 166–188.

Brochard-Wyart, F., Di Meglio, J.M., Quere, D. & De Gennes, P.G. 1991 Spreading of nonvolatile liquids in a continuum picture. *Langmuir* **7** (2), 335–338.

Buff, F.P. & Saltsburg, H. 1957 Curved fluid interfaces. II. The generalized Neumann formula. *J. Chem. Phys.* **26** (1), 23–31.

Camp, D.W. & Berg, J.C. 1987 The spreading of oil on water in the surface-tension regime. *J. Fluid Mech.* **184**, 445–462.

Carlson, A., Kim, P., Amberg, G. & Stone, H.A. 2013 Short and long time drop dynamics on lubricated substrates. *Europhys. Lett.* **104** (3), 34008.

Carrasco-Fadanelli, V. & Castillo, R. 2019 Measurement of the force between uncharged colloidal particles trapped at a flat air/water interface. *Soft Matt.* **15**, 5815–5818.

Couder, Y., Fort, E., Gautier, C.H. & Boudaoud, A. 2005 From bouncing to floating: noncoalescence of drops on a fluid bath. *Phys. Rev. Lett.* **94** (17), 177801.

Daerr, A. & Mogne, A. 2016 Pendent_drop: an ImageJ plugin to measure the surface tension from an image of a pendent drop. *J. Open Res. Softw.* **4**, e3.

Di Pietro, N.D., Huh, C. & Cox, R.G. 1978 The hydrodynamics of the spreading of one liquid on the surface of another. *J. Fluid Mech.* **84** (3), 529–549.

Ducloué, L., Hazel, A.L., Pihler-Puzović, D. & Juel, A. 2017 Viscous fingering and dendritic growth under an elastic membrane. *J. Fluid Mech.* **826**, R2.

Fay, J.A. 1969 *The Spread of Oil Slicks on a Calm Sea*, pp. 53–63. Springer.

Fingas, M. & Fieldhouse, B. 2012 Studies on water-in-oil products from crude oils and petroleum products. *Mar. Pollut. Bull.* **64** (2), 272–283.

Foda, M.A. & Cox, R.G. 1980 The spreading of thin liquid films on a water-air interface. *J. Fluid Mech.* **101**, 33–51.

Galatola, P. & Fournier, J.-B. 2014 Capillary force acting on a colloidal particle floating on a deformed interface. *Soft Matt.* **10**, 2197–2212.

Hadamard, J.S. 1911 Mouvement permanent lent d'une sphère liquid et visqueuse dans un liquide visqueux. *C. R. Acad. Sci.* **152**, 1735–1738.

HARKINS, W.D. 1941 A general thermodynamic theory of the spreading of liquids to form duplex films and of liquids or solids to form monolayers. *J. Chem. Phys.* **9** (7), 552–568.
JUEL, A., PIHLER-PUZOVIĆ, D. & HEIL, M. 2018 Instabilities in blistering. *Annu. Rev. Fluid Mech.* **50**, 691–714.
KANT, P., HAZEL, A.L., DOWLING, M., THOMPSON, A.B. & JUEL, A. 2017 Controlling droplet spreading with topography. *Phys. Rev. Fluids* **2**, 094002.
KARAPETSAS, G., CRASTER, R.V. & MATAR, O.K. 2011 Surfactant-driven dynamics of liquid lenses. *Phys. Fluids* **23** (12), 122106.
KELLAY, H., MEUNIER, J. & BINKS, B.P. 1992 Wetting properties of n-alkanes on AOT monolayers at the brine-air interface. *Phys. Rev. Lett.* **69**, 1220–1223.
KELLER, J.B. 1998 Surface tension force on a partly submerged body. *Phys. Fluids* **10** (11), 3009–3010.
KLEIDIENST, S., PAUL, J.H. & JOYE, S.B. 2015 Using dispersants after oil spills: impacts on the composition and activity of microbial communities. *Nat. Rev. Microbiol.* **13**, 388–396.
KRALCHEVSKY, P.A. & NAGAYAMA, K. 2000 Capillary interactions between particles bound to interfaces, liquid films and biomembranes. *Adv. Colloid Interface Sci.* **85** (2), 145–192.
LANDAU, L. & LEVICH, B. 1942 Dragging of a liquid by a moving plate. *Acta Physiochim. USSR* **17**, 42–54.
LANGMUIR, I. 1933 Oil lenses on water and the nature of monomolecular expanded films. *J. Chem. Phys.* **1** (11), 756–776.
LISTER, J.R., PENG, G.G. & NEUFELD, J.A. 2013 Viscous control of peeling an elastic sheet by bending and pulling. *Phys. Rev. Lett.* **111**, 154501.
MCGORTY, R., FUNG, J., KAZ, D. & MANOHARAN, V.N. 2010 Colloidal self-assembly at an interface. *Mater. Today* **13** (6), 34–42.
MCHALE, G., ORME, B.V., WELLS, G.G. & LEDESMA-AGUILAR, R. 2019 Apparent contact angles on lubricant-impregnated surfaces/SLIPS: from superhydrophobicity to electrowetting. *Langmuir* **35** (11), 4197–4204.
NAPOLI, G. & GORIELY, A. 2020 Elastocytosis. *J. Mech. Phys. Solids* **145**, 104133.
PARK, B.J. & FURST, E.M. 2010 Fluid-interface templating of two-dimensional colloidal crystals. *Soft Matt.* **6**, 485–488.
PHAN, C.M., ALLEN, B., PETERS, L.B., LE, T.N. & TADE, M.O. 2012 Can water float on oil? *Langmuir* **28** (10), 4609–4613.
PHAN, C.M., ALLEN, B., PETERS, L.B., LE, T.N. & TADE, M.O. 2014 Stability of a floating water droplet on an oil surface. *Langmuir* **30** (3), 0743–7463.
PROTIÈRE, S., JOSSERAND, C., ARISTOFF, J.M., STONE, H.A. & ABKARIAN, M. 2017 Sinking a granular raft. *Phys. Rev. Lett.* **118**, 108001.
RICHARD, D. & QUÉRÉ, D. 2000 Bouncing water drops. *Europhys. Lett.* **50** (6), 769–775.
RYBCZNSKI, W. 1911 Über die fortschreitende Bewegung einer flüssigen Kugel in einem zähen Medium. *Bull. Acad. Sci. Cracovie A.* 40–60.
SANJAY, V., JAIN, U., JALAAL, M., VAN DER MEER, D. & LOHSE, D. 2019 Droplet encapsulation. In *APS Division of Fluid Dynamics Meeting Abstracts*, p. B22.001.
SCHELLENBERGER, F., XIE, J., ENCINAS, N., HARDY, A., KLAPPER, M., PAPADOPOULOS, P., BUTT, H.J. & VOLLMER, D. 2015 Direct observation of drops on slippery lubricant-infused surfaces. *Soft Matt.* **11**, 7617–7626.
SETT, S., YAN, X., BARAC, G., BOLTON, L.W. & MILJKOVIĆ, N. 2017 Lubricant-infused surfaces for low-surface-tension fluids: promise versus reality. *ACS Appl. Mater. Interfaces* **9**, 36400–36408.
SMITH, J.D., DHIMAN, R., ANAND, S., REZA-GARDUNO, E., COHEN, R.E., MCKINLEY, G.H. & VARANASI, K.K. 2013 Droplet mobility on lubricant-impregnated surfaces. *Soft Matt.* **9**, 1772–1780.
SOLOMON, B.R., SUBRAMANYAM, S.B., FARNHAM, T.A., KHALIL, K.S., ANAND, S. & VARANASI, K.K. 2017 Chapter 10 Lubricant-impregnated surfaces. In *Non-wettable Surfaces: Theory, Preparation and Applications*, pp. 285–318. Royal Society of Chemistry.
TAYLOR, T.D. & ACRIVOS, A. 1964 On the deformation and drag of a falling viscous drop at low Reynolds number. *J. Fluid Mech.* **18** (3), 466–476.
THORODDSEN, S.T., THORAVAL, M.J., TAKEHARA, K. & ETOH, T.G. 2012 Micro-bubble morphologies following drop impacts on to a pool surface. *J. Fluid Mech.* **708**, 469–479.
TRAN, T., DE MALEPRADE, H., SUN, C. & LOHSE, D. 2013 Air entrainment during impact of droplets on liquid surfaces. *J. Fluid Mech.* **726**, R3.
VELLA, D. 2015 Floating versus sinking. *Annu. Rev. Fluid Mech.* **47** (1), 115–135.
VELLA, D., AUSSILLOUS, P. & MAHADEVAN, L. 2004 Elasticity of an interfacial particle raft. *Europhys. Lett.* **68** (2), 212–218.
VELLA, D. & MAHADEVAN, L. 2005 The 'Cheerios effect'. *Am. J. Phys.* **73** (9), 817–825.

WANG, B., WANG, C., YU, Y. & CHEN, X. 2020 Spreading and penetration of a micro-sized water droplet impacting onto oil layers. *Phys. Fluids* **32** (1), 012003.

WONG, C.Y.H., ADDA-BEDIA, M. & VELLA, D. 2017 Non-wetting drops at liquid interfaces: from liquid marbles to Leidenfrost drops. *Soft Matt.* **13**, 5250–5260.

YEO, Y., BASARAN, O.A & PARK, K. 2003 A new process for making reservoir-type microcapsules using ink-jet technology and interfacial phase separation. *J. Control. Release* **93** (2), 161–173.